Arp2/3-branched actin regulates microtubule acetylation level

and affects mitochondrial distribution

Peng Shi[1#], Yuan Wang[1#], Yuxing Huang[1], Chunlei Zhang[1], Ying Li[2], Yaoping Liu[3], Tingting Li[2], Wei Wang[3], Xin Liang[4], Congying Wu[1*]

[1] Institute of Systems Biomedicine, [2] Department of Biomedical Informatics, School of Basic Medical Sciences, Peking University Health Science Center, Beijing 100191, China. [3] Institute of Microelectronics, Peking University, Beijing, 100871, China [4] Tsinghua-Peking Joint Center for Life Sciences and Max-Plank Partner Group, School of Life Science, Tsinghua University, Beijing 100084, China

[#]These authors contribute equally to this work.

*Lead author: congyingwu@hsc.pku.edu.cn

Abstract

Actin and microtubule cytoskeletons regulate cell morphology, participate in organelle trafficking and function in response to diverse environmental cues. Precise spatial-temporal coordination between these two cytoskeletons is essential for cells to live and move. Here we report a novel cross-talk between actin and microtubules, in which the branched actin maintains microtubule organization, dynamics and stability by affecting tubulin acetylation level. We observe that acetylated tubulin significantly decreases upon perturbation of the Arp2/3-branched actin. We subsequently discover that HDAC6 participates in this process by altering its interaction with tubulin and the Arp2/3-stabilizer cortactin. We further identify that the homeostasis of branched actin controls mitochondrial distribution via this microtubule acetylation dependent mechanism. Our findings shed new light on the integral view of cytoskeletal networks, highlighting post-translational modification as another possible form of cytoskeletal inter-regulation, aside from the established cross-talks through structural connection or upstream signaling pathways.

Keywords: microtubule acetylation, Arp2/3-branched actin, HDAC6, cortactin, mitochondria.

Introduction

Actin filaments and microtubules orchestrate in numerous cellular processes under precise spatial-temporal control. Two major interactions–structural and regulatory, exist between these two cytoskeletons (Rodriguez et al., 2003). On one hand, linker proteins (e.g. ACF7) and motors mediate the static and dynamic structural associations respectively (Rodriguez et al., 2003). On the other hand, the dynamics of actin and microtubules feeds back to upstream signaling cascades, including small GTPases such as RhoA and Rac1, to indirectly affect each other (Palazzo et al., 2001, Wittmann and Waterman-Storer, 2001, Krendel et al., 2002, Boscheron et al., 2016, Andrieux et al., 2017). Recently, the connection between actin and microtubule post-translational modifications (PTM) has been suggested as another form of inter-cytoskeletal cross-talk (Fernandez-Barrera et al., 2018).

Microtubules are post-transcriptionally regulated and tubulins are among the most heavily modified proteins in the cytoplasm (Janke and Montagnac, 2017). Extensive studies over the past decade have identified multiple forms of PTMs on tubulins (Janke, 2014, Magiera and Janke, 2014, Song and Brady, 2015), which act as "tubulin code" to affect microtubule stability and motor behavior (Janke and Bulinski, 2011, Matov et al., 2010). Among them, tubulin acetylation has been reported to promote binding and motility of both kinesin and dynein motors on microtubules (Reed et al., 2006, Dompierre et al., 2007). Acetylation of microtubules is balanced by tubulin acetyltransferases and deacetylases (Hubbert et al., 2002, Castro-Castro et al., 2012, Akella et al., 2010). Inhibition of HDAC6, a major microtubule deacetylase, can rescue defects in Huntington's disease via increasing tubulin acetylation (Dompierre et al., 2007). Intriguingly, acetylated α-tubulin is most abundant in stable microtubules but is absent from dynamic cellular structures such as neuronal growth cones and the cell leading edge, where the Arp2/3-branched actin dependent protrusion-lamellipodia are highly active (Portran et al., 2017, Song and Brady, 2015, Hammond et al., 2008).

The actin network is composed of branched and linear forms of filaments. The Arp2/3 complex binds to pre-existing mother filaments and nucleates branched actin with a 70 degree angle, creating a dense meshwork at the peri-membranous regions (Goley and Welch, 2006, Rotty et al., 2013, Pollard and Cooper, 2009). Branched actin also controls local trafficking of intracellular vesicles, confining axonal transport of myosin V cargos (Balasanyan et al., 2017). Cortactin, an actin filament-binding protein and target of multiple kinases, serves to stabilize actin branches and as a weak nucleation promoting factor by simultaneous binding F-actin and Arp2/3 (Weaver et al., 2001, Uruno et al., 2001). Interestingly, cortactin has been identified to be another important substrate of HDAC6 (Zhang et al., 2007). Acetylated cortactin translocates from the cell leading edge and resides in the cytoplasm (Ito et al., 2015). Interestingly, HDAC6 has also been reported to enhance directional cell migration-a process

heavily relying on branched actin dynamics (Hubbert et al., 2002). However, whether acetylated microtubules structurally or functionally associate with branched actin in various cellular processes remains elusive.

In this study, we observe a novel cross-talk between the branched actin and microtubules, in which perturbation of the Arp2/3-branched actin affects microtubule architecture, dynamics and stability. We identify the underlying mechanisms to involve cortactin in biasing HDAC6 association and activity, thus affecting tubulin acetylation level. We also report the involvement of this cross-talk in subcellular distribution of mitochondria, possibly by affecting kinesin and dynein motors.

Results

Branched actin affects microtubule architecture, dynamics and stability

Arp2/3 inhibition by CK-666 (Hetrick et al., 2013) resulted in cells lacking lamellipodia (Wu et al., 2012, Suraneni et al., 2012). These cells align thick bundles of actin filaments along the cell periphery (Fig. S1A), the region where microtubules in a normal cell encounter plasma membrane and reverse (Rotty et al., 2015) (Fig. S1B). We thus wondered whether loss of branched actin would affect microtubule organization and architecture. Airyscan confocal microscopy and Structured Illumination Microscopy (SIM) were employed to reveal individual microtubule filaments in fixed cells. Interestingly, we observed less complex microtubule networks in the Arp2/3-inhibited cells (Fig. 1A & S1C). To quantify this observation, we first defined filament joint as points where two or more microtubule filaments cross one another (Fig. S1C & methods). Then we manually identified filament joints from the super-resolution images and quantified the joint number per cell (Fig. 1A) or per area (Fig. S1C) to reveal network complexity (Zhang et al., 2017) (see methods). Reduced microtubule complexity was obvious in Arp2/3-inhibited cells, indicating that microtubule organization responded to branched actin alteration. We then evaluated microtubule dynamics by analyzing the trajectories of the growing end binding protein EB1 (Matov et al., 2010), which indicate the growing microtubules (Wittmann et al., 2003, Henty-Ridilla et al., 2016). Microtubule plus ends extended and turned back towards the cell body in normal cells, but EB1 tracks showed fewer returns in Arp2/3-inhibited cells (Fig. 1B, I & Movies S1-S2). Consistently, the EB1 persistence was higher at the cell periphery in Arp2/3-inhibited cells (Fig. 1B, III & IV). Interestingly, we observed decreased EB1 velocity upon disruption of branched actin (Fig. 1B, II), indicative of reduced microtubule growth rate. Aside from the changes in microtubule organization and dynamics, we also detected decreased microtubule stability when Arp2/3-branched actin was inhibited. The whole microtubule network in the Arp2/3-inhibited cells appeared collapsed under the cold PBS treatment when regions of intact microtubules were still visible with normal cells (Fig. 1C). Moreover, perturbing the branched actin enhanced microtubule depolymerization under nocodazole treatment (Fig. 1D). Therefore, disrupting the Arp2/3-branched actin reduced microtubule dynamics and stability, creating less complex microtubule network within the cell.

Perturbation of the Arp2/3-branched actin decreases microtubule acetylation level through HDAC6

Changes in cold and nocodazole stability oftentimes reveal alterations in microtubule PTM states (Song et al., 2013, Billger et al., 1991). Highly acetylated microtubules have been reported to be cold and nocodazole resistant (Xu et al., 2017). Microtubule acetylation has been shown to associate with long-lived filaments, which were highly interconnected (Portran et al., 2017, Kalebic et al., 2013). Enhancing microtubule acetylation also affects the speed of EB1 comets in vivo (Matov et al., 2010). We hence

suspected that microtubule PTMs were changed upon disruption of the Arp2/3-branched actin, resulting in altered microtubule organization, dynamics and stability.

By immunoblotting, we indeed detected significant decrease in acetylated tubulin in Arp2/3-deleted cells (Fig. 2A & S2D, a). Similar result showing reduced tubulin acetylation level but not tyrosination or detyrosination was revealed by transiently inhibiting the Arp2/3 activity using CK-666 (Fig. 2B, 2C & S2D, b-c). Immunofluorescent staining and subsequent quantification confirmed these results (Fig. 2D). When we specifically inhibited the major tubulin deacetylase HDAC6 by Tubacin, we no longer detected reduction in acetylated tubulin upon CK-666 treatment (Fig. 2E, S2A & S2D, d). While under the treatment of sodium butyrate (NaB), a class I HDACs inhibitor that does not inhibit HDAC6, we still observed reduction in acetylated tubulin upon Arp2/3 inhibition (Fig. 2E & 2F). Although been reported to contribute to microtubule deacetylation in certain cells, SIRT1/2 inhibition by Tenovin-6 showed marginal effects on acetylated tubulin level in our system, excluding them being the lead tubulin deacetylase in cells that we used (Fig. 2F & S2D, e). Additionally, unlike HDAC6 inhibition by Tubacin, Tenovin-6 did not rescue CK-666 induced reduction of acetylated tubulin (Fig. 2F & S2D, e), indicating that SIRT1/2 were not essential in this process. Interestingly, we observed rescuing effects on microtubule complexity and dynamics when Tubacin was applied to Arp2/3-inhibited cells (Fig. S2B, S2C & Movies S3). We then asked how HDAC6 responded to the branched actin alterations.

HDAC6 balances cortactin and tubulin acetylation levels to orchestrate branched actin and microtubule cytoskeletons

Aside from being a major tubulin deacetylase, HDAC6 also regulates the deacetylation of the Arp2/3-associated protein cortactin (Zhang et al., 2007, Castro-Castro et al., 2012). We performed the co-occurrence analysis (Li et al., 2017) of α-tubulin and cortactin acetylation sites (Fig. S3A & S3B), and found significant co-occurrent association of acetylation on α-tubulin K40 and three sites on cortactin (K124, K161 and K309). This implicated functional association between α-tubulin and cortactin acetylation and that the acetylation on both proteins may be correlated.

We then evaluated the effects on cortactin acetylation level by Arp2/3 inhibition. Interestingly, acetylated cortactin showed a time-dependent increase in response to CK-666 treatment (Fig. 3A & S2D, f), opposite to what we observed with acetylated tubulin (Fig. 2B & 2C). Decrease in acetylated tubulin upon Arp2/3 inhibition was largely dependent on HDAC6 (Fig. 2E). Additionally, inhibition of HDAC6 also aborted the increase in acetylated cortactin upon branched actin disruption (Fig. 3B & S2D, g). This "seesaw" effect with tubulin and cortactin acetylation levels suggested an intriguing competition mechanism involving HDAC6.

We wondered whether the localization and/or activity of HDAC6 changed under Arp2/3-branched

actin disruption. Since HDAC6 showed a relatively diffusive cytoplasmic distribution in cells (Hubbert et al., 2002), we employed a BiFC system (Shyu et al., 2006) to detect any specially localized HDAC6/cortactin interaction sites in live cells. We observed bright signals at the cell leading edge and cytoplasm, suggesting localization-specific interactions between these two proteins (Fig. 3C & S3C). As a negative control, we expressed one half of the split GFP tagged to cortactin and the other half without HDAC6 in cells, and detected no fluorescent signal (Fig. 4D). To further eliminate non-specific effects, we generated cells expressing split halves of GFP tagged to HDAC6 and WAVE1 that also enriched in lamellipodia. No positive signals were detected at cell leading edge or cytoplasm (Fig. S3D). To test the possible affinity changes between HDAC6/cortactin and HDAC6/α-tubulin upon loss of branched actin, we used the proximity ligation assay (PLA) in control or CK-666 treated cells. We detected reduced number of positive PLA sites between HDAC6 and cortactin under Arp2/3 inhibition, and observed specific disappearance of spots at cell periphery (Fig. 3D & 3F), indicative of loss of leading-edge HDAC6/cortactin interaction. Meanwhile, increased number of HDAC6/α-tubulin sites were revealed upon CK-666 treatment (Fig. 3E & 3F). Both negative and positive controls were considered in these PLA assays (Fig. S3E). The competition mechanism predicted that if cortactin was absent, tubulin acetylation level would increase; and that cortactin-depleted cells would not respond to CK-666 in further decreasing acetylated tubulin. Our experiments agreed well with these predictions (Fig. 3G), supporting the above competition model.

Arp2/3-branched actin regulates mitochondrial distribution through changes in tubulin acetylation level

Both actin and microtubule cytoskeletons participate in the distribution and function of cellular organelles. It has been suggested that a cooperative regulation exists between actin/microtubule-based mitochondrial dynamics (Pathak et al., 2010, Morris and Hollenbeck, 1995, Lopez-Domenech et al., 2018). Mitochondrial morphology and distribution affect multiple cellular physiological processes including synaptic homeostasis, neurodegeneration and cell migration (Sheng and Cai, 2012, Schuler et al., 2017). However, how actin and microtubule cooperatively regulate mitochondrial network is largely unknown. We noticed that mitochondria expanded to the cell periphery in Arp2/3-inhibited cells (Fig. 4A, Movies S4-S5). To better control cell morphology and polarity, we micro-patterned extracellular matrix (2000 µm² triangle shape) to ensure sufficient cell spreading while normalizing cell shape and area (Chevrollier et al., 2012). In this setting, expansion of mitochondrial distribution was also observed (Fig. S4A). Interestingly, this mitochondrial distribution change was absent when high concentration of nocodazole was applied (Fig. 4B, S4A & Movies S6-S7), suggesting its dependency on microtubule integrity. We then asked whether microtubule acetylation involved in this branched actin-

regulated mitochondrial expansion. Interestingly, when we inhibited HDAC6 to increase tubulin acetylation level, mitochondrial distribution remained unchanged instead of expanded to the cell periphery upon Arp2/3 inhibition (Fig 4C, S4A & Movies S8-S9). Consistently, we observed increased mitochondrial area when HDAC6 was overexpressed, similar to what was observed in branched actin-disrupted cells (Fig. S4B).

Then we asked how altered microtubule acetylation level affects the dynamic distribution of mitochondria. Previous studies demonstrated that kinesin-1 played a major role in driving the anterograde transport of mitochondria in the cell and the retrograde transport of mitochondria is driven by dynein (Nangaku et al., 1994). Consistent with previous reports, when we depleted Kif5b, mitochondria shrank back to the pre-nuclear regions (Fig. 4D & S4C). Moreover, when we inhibited HDAC6 or Arp2/3 in these Kif5b knock-out cells, we observed unchanged mitochondrial distribution (Fig. 4D & S4C). These results suggested that kinesin-1 played a crucial role in tubulin acetylation regulated mitochondrial distribution. This is counterintuitive because tubulin acetylation was reported to promote the activities of kinesin-1 motor in vivo (Dompierre et al., 2007, Reed et al., 2006). The dynein motor, on the other hand, has an retrograde activity and is activated by tubulin acetylation (Alper et al., 2014) have a reduced activity that leads to mitochondrial expansion. We thus supposed that the reduction of microtubule acetylation reduced Kinesin-1 activity and would induced a peri-nuclear mitochondrial distribution. Indeed, when we used the cytoplasmic dynein inhibitor ciliobrevins D (Cilio D) to treat cells, the mitochondria expanded to the cell periphery (Fig. 4E & S4D) , consistent with previous findings (Firestone et al., 2012). Next, we combined Cilio D with tubacin, and consistent with our hypothesis, we detected expansion of mitochondrial distribution to the cell periphery (Fig. 4E & S4D). These results suggested that the altered microtubule acetylation level affected mitochondrial distribution through tilting the tugging balance between kinesin and dynein motors. And the different sensibility for kinesin and dynein to microtubule acetylation may determine the dynamic distribution of mitochondria.

Discussions

Numerous cellular processes require both the actin filaments and microtubules to coordinate precisely in space and time. Long-lived microtubules are oftentimes acetylated, enabling long-range cargo transport (Portran et al., 2017, Xu et al., 2017), while local reorganization of specific forms of actin filaments modulates the fine control of their distributions (Balasanyan et al., 2017). We report here an unanticipated regulation from branched actin to microtubules, in which disruption of the branched/linear actin ratio triggers cortactin dissociation from the leading edge and causes its affinity with HDAC6 to decrease, leading to enhanced HDAC6-tubulin association and reduction in tubulin

acetylation level (Fig. 4F, a). This mechanism participates in Arp2/3-mediated mitochondrial distribution change, in which loss of Arp2/3 leads to expansion of mitochondrial occupancy (Fig.4F, b). The expansion in mitochondrial distribution upon disruption of Arp2/3-branched actin is microtubule dependent and is fully rescued when manipulating HDAC6 activity. Recent observation on Kif5b knockout cells has shown that depletion of this kinesin restricts mitochondria to peri-nucleus area, indicating its role in mediating the outward movement and meshwork formation of mitochondria (Wang et al., 2015).

Cortactin is regarded as a central pillar connecting signaling pathways with cytoskeletal remodeling. We show in this study that the leading edge localization of cortactin largely depends on the integrity of the branched actin. Dissociation of cortactin from the branched actin induced by Arp2/3-inhibition significantly disrupts its interaction with HDAC6 while allowing more tubulin-HDAC6 binding. Cells depleted of cortactin enhances tubulin deacetylation, supporting a competition between cortactin and tubulin for HDAC6 activity. A competition mechanism suggests a mutual factor to be limited in abundance. It has been shown by exogenously expressing GFP-HDAC6 or by immunofluorescent labeling the endogenous protein that HDAC6 resides in a diffusive manner in the cytoplasm with a small portion at the cell leading edge (Hubbert et al., 2002). This relatively low specific cytoplasmic localization of HDAC6 seems to argue against it being a limiting enzyme. However, as cortactin harbors nine lysine acetylation sites (Zhang et al., 2007) and tubulin is very abundant (~10 μM) in the cytosol (Henty-Ridilla et al., 2017). These two components may well compete for the same pool of this deacetylase under certain conditions.

Actin and microtubule cytoskeletons act coordinately during cell migration. In wound healing, microtubules and actin synergistically form radial array around the wound edge (Mandato and Bement, 2003, Mandato and Bement, 2001). Intact microtubule cytoskeleton was required to maintain polarized distribution of actin-dependent protrusions at the leading edge of migrating fibroblasts (Waterman-Storer et al., 1999). Moreover, both microtubule PTM and actin homeostasis involve in neuronal morphogenesis. How branched actin and acetylated microtubule work together in axon branching and growth cone guidance is tentative to view from a new perspective of cytoskeletal crosstalk. With more interconnected regulations among different cytoskeletons investigated, our understanding of the effect on microtubule acetylation from branched actin will facilitate and expedite comprehensive studies of cellular morphology and function.

One intriguing question would be to ask whether a reversed process exists, in which perturbation of tubulin acetylation remodels branched actin. Assaying Arp2/3 complex or cortactin localization when manipulating tubulin acetylation level will help test this hypothesis. Comprehensive biochemical and structural studies will greatly facilitate the understanding of a potential bidirectional regulation

between branched actin and tubulin acetylation. However, as cortactin harbors nine lysine acetylation sites in its repeat region, a dampening mechanism may exist to interfere with the regulation from tubulin acetylation to branched actin. It has been reported recently that INF2 loss induces reduction of microtubule acetylation due to the down regulation of α-TAT1 through actin-MRTF-SRF circuit (Fernandez-Barrera et al., 2018). These together with our findings add another layer to the inter-regulations between different cytoskeletons. Whether other forms of PTM-based cross-connections exist may be of great interest to the field.

Another evidence that must be considered is that HDAC6 and cortactin are both involved in tumor progression(Aldana-Masangkay and Sakamoto, 2011, Ammer and Weed, 2008) . Whether tubulin acetylation level or branched actin organization associate with this scenario is worth evaluating. It is challenging yet important to investigate the role of PTM mediated cytoskeletal cross-talk in tumor proliferation and invasive migration. Altered tubulin acetylation level involves in a number of pathological conditions, such as familial dysautonomia and Alzheimer's, Huntington's, and Charcot-Marie-Tooth diseases (Hempen and Brion, 1996, Dompierre et al., 2007, Gardiner et al., 2007, d'Ydewalle et al., 2011). Elucidating potential cytoskeletal cross-regulations (Jiu et al., 2015) and extracting critical regulators to target under pathological conditions, may serve as one stone to hit multiple complex but coordinated processes.

Author Contributions

C.W., P.S. and Y.W. conceived the project and designed the experiments. P.S. and Y.W. performed the imaging experiments and data analysis. Y.H. constructed stable cell lines. C.Z. assisted with plasmid construction. Y.L. conducted bioinformatic analysis. P.S., Y.W. and C.W. wrote the manuscript, with inputs from X.L., and T.L.. All authors participated in discussion and editing of the manuscript.

Competing financial interests

The authors declare no competing financial interests.

Materials and methods

Antibodies and reagents

The following antibodies were used in this study: anti-α-tubulin (T9026), anti-acetyl-tubulin (T7451), anti-HDAC6 (HPA026321) from Sigma-Aldrich; anti-cortactin (05-180), anti-acetyl-cortactin (09-881), anti-ARPC2 (07-227), anti-non-tyrosinated-tubulin (ABT170), anti-tyrosinated-tubulin (ABT171) from EMD Millipore; anti-GFP (598) from MBL, anti-mouse (sc-2005) and anti-rabbit (sc-2004) HRP conjugated secondary antibodies from Santa Cruz. HDAC6 inhibitor (Tubacin,SML0065), the Arp2/3 complex inhibitor (CK-666, 182515) and cytoplasmic dynein inhibitor (Ciliobrevin D, 250401) were purchased from EMD Millipore. SIRT1/2 inhibitor Tenovin-6 (S4900) was from Selleck Chemicals. Nocodazole (M1404), 4-Hydroxytamoxifen, Sodium butyrate (NaB), and puromycin (P8833) were obtained from Sigma-Aldrich. Mitotracker (M7512) was obtained from Thermo Fisher.

Cell lines and cell culture

Mouse embryonic fibroblasts (MEFs) and Human embryonic kidney cells 293T (HEK 293T) were kept by our laboratory. Human retinal pigment epithelium (RPE cell) and KIF5B knockout RPE cells were generously provided by V. Gelfand (Northwestern University, Chicago). Inducible ARPC2 knockout MEFs were generously provided by James E. Bear laboratory (UNC-Chapel Hill) and the induction protocol was described previously (Rotty *et al.*, 2015). Cells were cultured in DMEM media supplemented with 10% FBS (PAN, Biotech), 100 U/mL penicillin, and 100 μg/mL streptomycin at 37 ℃ with 5% CO_2.

Plasmids and transient transfection

GFP-cortactin (26722), cortactin-pmCherryC1 (27676), pEGFP.N1-HDAC6 (36188) pcDNA-HDAC6-flag (30482), pEB1-2xEGFP, pcDNA-HDAC6.DC-flag (30483) and LentiCRISPRv2 (52961) were obtained from Addgene. BiFC-VC155, BiFC-VN173 and Mito-YFP plasmids were generously provided by Yujie Sun laboratory (Peking University). Lifeact-GFP and Lifeact-RFP were generously provided by James E. Bear laboratory (UNC-Chapel Hill). Cortactin, HDAC6 and EB1-2xEGFP, Mito-YFP and Lifeact-RFP were sub cloned into lentiviral vector (Plvx-ac-GFP-N1) for establishing stable cell lines. Mouse WAVE1 was cloned from the mouse tissue extracted cDNA library. HEK 293T cells were transfected following the Neofect DNA transfection protocol (KS2000). After 24-48 h, cells were checked for fluorescent protein expression followed by imaging or harvesting cell lysates.

CRISPR Cas9 mediated Cortactin gene knockout

The following sgRNA and primers were used to generate cortactin knock-out MEFs:

Mouse sgRNA forward sgRNA-1 :5'-TCCTCCATCATCCTGCGTGA-3'

Mouse sgRNA forward sgRNA-2 :5'- GTGACTCCTACCACAAAATC-3'

Single cell clone from lentivirus infected pool cells was selected and verified by western blotting and DNA sequencing.

Western blotting

For western blotting, cells were washed with DPBS once and lysed in appropriate volume of RIPA buffer (50 mM Tris-HCl, pH8.0, 150 mM NaCl, 1% Triton X-100, 0.5% Na-deoxycholate, 0.1% SDS, 1 mM EDTA, and Protease Inhibitor Cocktail) for 10 min on ice. Lysates were centrifuged at 12000 rpm for 15 min and the supernatants were collected. 5 x SDS loading buffer was added to the supernatants and boiled for 10 min at 95 ℃. Protein samples were run on 10% SDS PAGE acrylamide gels and transferred onto PVDF membranes by wet electrophoretic transfer. Followed by the first and second antibody incubation at 4℃ overnight or room temperature for 2 h. The X-ray film was used to detect and record the bands intensity. The fixed X-ray film was scan and got the digital images. The images were processed by the Image J software (https://imagej.nih.gov/ij/). Images were first transferred to 8-bit depth. Then the intensity of bands was quantified by using image J (image J —> Analyze—>Gels). The intensity was normalized to GAPDH or α-tubulin. And plotted the graph as mean± 95% CI.

Proximity Ligation Assay

To detect the interaction between HDAC6 with cortactin or α-tubulin in vivo, the proximity ligation assay was performed with Duolink kits from Sigma-Aldrich. Cells expressing HDAC6-EGFP were treated with CK-666 followed by fixation with 4% paraformaldehyde at room temperature for 10 min. Then the cells were permeabilized with 0.5% Triton X-100 in PBS for 5 min, followed by 3 times wash with PBS. Commercial blocking solution was added to the samples to incubate for 1 h at room temperature. Mouse anti-cortactin or mouse anti-α-tubulin antibodies were mixed with Rabbit anti-GFP antibodies and diluted (1:200) in the antibody diluent. After removing the blocking solution, the diluted antibodies were incubated with cells for 1 h at room temperature followed by 3x 5 min wash in PBS. The PLUS and MINUS PLA probes were mixed and diluted (1:5) in antibody diluent and incubated with samples for 1 h at 37 ℃. Then the samples were washed in 1× Wash Buffer A for 2×5 min. The ligase was diluted (1:40) in diluted ligation buffer (1:5 in H_2O) and the mixture was incubated with samples for 1 h at 37 ℃. After washing the samples in 1× Wash Buffer A for 2×2 min, the polymerase was diluted (1:80) in diluted amplification stock (1:5 in H_2O) and the mix was incubated with samples for 100 min at 37 ℃. The samples were then washed in 1× Wash Buffer B for 2×10 min followed by another wash in 0.01× Wash Buffer B again for 1 min. Finally, the samples were mounted with Prolong Diamond Antifade with DAPI (P36962) for 30 min at room temperature.

For positive control of PLA experiments, anti-tyrosinated tubulin and anti-α-tubulin antibody were used to identify the positive signals. For negative control of PLA experiments, anti-cortactin and antiα-tubulin antibody were used.

Bimolecular fluorescence complementation (BiFC)

To perform BiFC assay, two proteins of interest fused with either Flag-VN173 of HA-VC155 were transferred to cells simultaneously. After 24 h, cells were fixed and stained for imaging using a Nikon A1R confocal microscope.

Structured illumination microscopy (SIM)

SIM imaging of fixed cells was performed using an N-SIM (Nikon) with a HP Apo TIRF 100× 1.49 NA oil objective lens. Three angles of the excitation grid with five phases each were acquired for each channel. SIM processing was performed using the SIM module of the NIS view software package. 16-bit grayscale tiffs were subsequently exported to Image J for quantification and processing into rendered colored images.

Immunofluorescence and imaging analysis

Cells were plated on acid-washed coverslips coated with 5 µg/mL fibronectin overnight. Cells were then fixed with 4% PFA at room temperature for 15 min or methanol at -20 ℃ for 25 min, permeabilized in 0.5% Triton X-100 in PBS for 10 min, washed with PBS once for 5 min and blocked with 5% BSA for 1 h. For cortactin staining, antibody was diluted 1:200 in 1% BSA (Sigma) and incubated for 1 h at room temperature. After 3 times washing with PBS, the coverslips were incubated with Alexa Fluor 488 secondary antibody (A-21202, Life) and phalloidin (PHDR1, Cytoskeleton) for 1 h at room temperature. After another 3 times PBS washing, the coverslips were mounted with Prolong Diamond Antifade with DAPI. Images were captured using a Nikon A1R confocal microscope.

Microtubule network complexity analysis

Image J was used to process all images and the microtubule network joints was counted manually. Microtubule joint was defined as the site where two or more microtubule filaments crossed one another. The number of microtubule joints were analyzed per area or per cell. The number of joints was referred as microtubule complexity (Zhang et al., 2017).

Acetylation co-occurrence analysis

We downloaded all experimentally observed human acetylation sites from the PhosphoSitePlus database (http://www.phosphosite.org). The observed modification sites were further stratified into different laboratory (cell line vs. tissue) and physiological (disease vs. non-disease) conditions, resulting in a total 33 data files. To ensure proteome-wide coverage, we only retained 21 different conditions with at least 400 modification sites.

For each pair of acetylation sites, we cross-tabulated the incidents that two residues are acetylated under different conditions into a 2-by-2 contingency table. The p-value of one-sided FET was used to evaluate the tendency of acetylation to co-occur under the same conditions.

Live-cell imaging

Live-cell images were acquired with a 60× 1.4 NA objective lens on a spinning disk confocal imaging system (Nikon Ti2-E). Cells were plated on fibronectin (10 µg/mL) coated glass bottom cell culture dish before imaging. For EB1-2XEGFP imaging, the interval was 2 seconds and the growth speed was analyzed by *plus Tiptracker (Matov et al., 2010)*. Cells were maintained in DMEM media supplemented with 10% FBS (PAN, Biotech), 100 U/mL penicillin, 100 µg/mL streptomycin at 37 ℃ throughout the imaging process. Images were acquired at indicated intervals.

For mitochondrial imaging, all buffers and reagents added were preheated to 37 ℃.

Statistics

The number of biological and technical replicates and the number of samples are indicated in figure legends, main text and Methods. Data are mean ± SEM or mean ± 95% CI as indicated in the legends of the figures and supplemental data figures. t-test and non-parametric test analysis were performed with GraphPad Prism 7.0. For the data of EB1 speed and persistence, we randomly selected 3000 for further non-parametric analysis.

Parylene C micropatterns

The fabrication of micropore-arrayed Parylene C membrane was schematically shown in Fig. S4E. First, a thin film (5 μm) of Parylene C was deposited on a 4-inch silicon wafer, followed by the spinning and UV lithography patterning of photoresist (8 μm-thick, AZ9260). After that, an oxygen plasma etching of Parylene C was performed with the patterned AZ 9260 as a mask, and then the wafer was immersed in PRS-3000 solution at 65℃ till the through removal of photoresist. Last, the prepared micropore-arrayed Parylene C membrane was released from the silicon wafer in deionized water bath.

To adhere the Parylene C membrane to glass coverslips, PDMS was coated on coverslips. Polydimethylsiloxane (PDMS, Sylgard 184) was mixed for 5 min with a monomer to curing agent ratio of 10:1, and then spin coated at 2000 rpm for 1 min. After adhering Parylene C membrane to PDMS, fibronectin was coated on the membrane to functionalize micropatterns. Then the Parylene C membrane was removed and cells were plated on fibronectin coated surface for 4-6 h. Cells were then fixed and imaged with a Nikon A1R confocal microscope.

Reference

Akella, J. S., Wloga, D., Kim, J., Starostina, N. G., Lyons-Abbott, S., Morrissette, N. S., Dougan, S. T., Kipreos, E. T. & Gaertig, J. 2010. MEC-17 is an alpha-tubulin acetyltransferase. *Nature,* 467, 218-22.

Aldana-Masangkay, G. I. & Sakamoto, K. M. 2011. The role of HDAC6 in cancer. *J Biomed Biotechnol,* 2011, 875824.

Alper, J. D., Decker, F., Agana, B. & Howard, J. 2014. The motility of axonemal dynein is regulated by the tubulin code. *Biophys J,* 107, 2872-2880.

Ammer, A. G. & Weed, S. A. 2008. Cortactin branches out: roles in regulating protrusive actin dynamics. *Cell Motil Cytoskeleton,* 65, 687-707.

Andrieux, A., Aubry, L. & Boscheron, C. 2017. CAP-Gly proteins contribute to microtubule-dependent trafficking via interactions with the C-terminal aromatic residue of alpha-tubulin. *Small GTPases*, 1-8.

Balasanyan, V., Watanabe, K., Dempsey, W. P., Lewis, T. L., Jr., Trinh, L. A. & Arnold, D. B. 2017. Structure and Function of an Actin-Based Filter in the Proximal Axon. *Cell Rep,* 21, 2696-2705.

Billger, M., Stromberg, E. & Wallin, M. 1991. Microtubule-associated proteins-dependent colchicine stability of acetylated cold-labile brain microtubules from the Atlantic cod, Gadus morhua. *J Cell Biol,* 113, 331-8.

Boscheron, C., Caudron, F., Loeillet, S., Peloso, C., Mugnier, M., Kurzawa, L., Nicolas, A., Denarier, E., Aubry, L. & Andrieux, A. 2016. A role for the yeast CLIP170 ortholog, the plus-end-tracking protein Bik1, and the Rho1 GTPase in Snc1 trafficking. *J Cell Sci,* 129, 3332-41.

Castro-Castro, A., Janke, C., Montagnac, G., Paul-Gilloteaux, P. & Chavrier, P. 2012. ATAT1/MEC-17 acetyltransferase and HDAC6 deacetylase control a balance of acetylation of alpha-tubulin and cortactin and regulate MT1-MMP trafficking and breast tumor cell invasion. *Eur J Cell Biol,* 91, 950-60.

Chevrollier, A., Cassereau, J., Ferre, M., Alban, J., Desquiret-Dumas, V., Gueguen, N., Amati-Bonneau, P., Procaccio, V., Bonneau, D. & Reynier, P. 2012. Standardized mitochondrial analysis gives new insights into mitochondrial dynamics and OPA1 function. *Int J Biochem Cell Biol,* 44, 980-8.

D'ydewalle, C., Krishnan, J., Chiheb, D. M., Van Damme, P., Irobi, J., Kozikowski, A. P., Vanden Berghe, P., Timmerman, V., Robberecht, W. & Van Den Bosch, L. 2011. HDAC6 inhibitors reverse axonal loss in a mouse model of mutant HSPB1-induced Charcot-Marie-Tooth disease. *Nat Med,* 17, 968-74.

Dompierre, J. P., Godin, J. D., Charrin, B. C., Cordelieres, F. P., King, S. J., Humbert, S. & Saudou, F.

2007. Histone deacetylase 6 inhibition compensates for the transport deficit in Huntington's disease by increasing tubulin acetylation. *J Neurosci,* 27, 3571-83.

Fernandez-Barrera, J., Bernabe-Rubio, M., Casares-Arias, J., Rangel, L., Fernandez-Martin, L., Correas, I. & Alonso, M. A. 2018. The actin-MRTF-SRF transcriptional circuit controls tubulin acetylation via alpha-TAT1 gene expression. *J Cell Biol.*

Firestone, A. J., Weinger, J. S., Maldonado, M., Barlan, K., Langston, L. D., O'donnell, M., Gelfand, V. I., Kapoor, T. M. & Chen, J. K. 2012. Small-molecule inhibitors of the AAA+ ATPase motor cytoplasmic dynein. *Nature,* 484, 125-9.

Gardiner, J., Barton, D., Marc, J. & Overall, R. 2007. Potential role of tubulin acetylation and microtubule-based protein trafficking in familial dysautonomia. *Traffic,* 8, 1145-9.

Goley, E. D. & Welch, M. D. 2006. The ARP2/3 complex: an actin nucleator comes of age. *Nat Rev Mol Cell Biol,* 7, 713-26.

Hammond, J. W., Cai, D. & Verhey, K. J. 2008. Tubulin modifications and their cellular functions. *Curr Opin Cell Biol,* 20, 71-6.

Hempen, B. & Brion, J. P. 1996. Reduction of acetylated alpha-tubulin immunoreactivity in neurofibrillary tangle-bearing neurons in Alzheimer's disease. *J Neuropathol Exp Neurol,* 55, 964-72.

Henty-Ridilla, J. L., Juanes, M. A. & Goode, B. L. 2017. Profilin Directly Promotes Microtubule Growth through Residues Mutated in Amyotrophic Lateral Sclerosis. *Curr Biol,* 27, 3535-3543 e4.

Henty-Ridilla, J. L., Rankova, A., Eskin, J. A., Kenny, K. & Goode, B. L. 2016. Accelerated actin filament polymerization from microtubule plus ends. *Science,* 352, 1004-9.

Hetrick, B., Han, M. S., Helgeson, L. A. & Nolen, B. J. 2013. Small molecules CK-666 and CK-869 inhibit actin-related protein 2/3 complex by blocking an activating conformational change. *Chem Biol,* 20, 701-12.

Hubbert, C., Guardiola, A., Shao, R., Kawaguchi, Y., Ito, A., Nixon, A., Yoshida, M., Wang, X. F. & Yao, T. P. 2002. HDAC6 is a microtubule-associated deacetylase. *Nature,* 417, 455-8.

Ito, A., Shimazu, T., Maeda, S., Shah, A. A., Tsunoda, T., Iemura, S., Natsume, T., Suzuki, T., Motohashi, H., Yamamoto, M. & Yoshida, M. 2015. The subcellular localization and activity of cortactin is regulated by acetylation and interaction with Keap1. *Sci Signal,* 8, ra120.

Janke, C. 2014. The tubulin code: molecular components, readout mechanisms, and functions. *J Cell Biol,* 206, 461-72.

Janke, C. & Bulinski, J. C. 2011. Post-translational regulation of the microtubule cytoskeleton: mechanisms and functions. *Nat Rev Mol Cell Biol,* 12, 773-86.

Janke, C. & Montagnac, G. 2017. Causes and Consequences of Microtubule Acetylation. *Curr Biol,* 27, R1287-R1292.

Jiu, Y. M., Lehtimaki, J., Tojkander, S., Cheng, F., Jaalinoja, H., Liu, X. N., Varjosalo, M., Eriksson, J. E. & Lappalainen, P. 2015. Bidirectional Interplay between Vimentin Intermediate Filaments and Contractile Actin Stress Fibers. *Cell Reports,* 11, 1511-1518.

Kalebic, N., Martinez, C., Perlas, E., Hublitz, P., Bilbao-Cortes, D., Fiedorczuk, K., Andolfo, A. & Heppenstall, P. A. 2013. Tubulin acetyltransferase alphaTAT1 destabilizes microtubules independently of its acetylation activity. *Mol Cell Biol,* 33, 1114-23.

Krendel, M., Zenke, F. T. & Bokoch, G. M. 2002. Nucleotide exchange factor GEF-H1 mediates cross-talk between microtubules and the actin cytoskeleton. *Nat Cell Biol,* 4, 294-301.

Li, Y., Zhou, X., Zhai, Z. & Li, T. 2017. Co-occurring protein phosphorylation are functionally associated. *PLoS Comput Biol,* 13, e1005502.

Lopez-Domenech, G., Covill-Cooke, C., Ivankovic, D., Halff, E. F., Sheehan, D. F., Norkett, R., Birsa, N. & Kittler, J. T. 2018. Miro proteins coordinate microtubule- and actin-dependent mitochondrial transport and distribution. *EMBO J,* 37, 321-336.

Magiera, M. M. & Janke, C. 2014. Post-translational modifications of tubulin. *Curr Biol,* 24, R351-4.

Mandato, C. A. & Bement, W. M. 2001. Contraction and polymerization cooperate to assemble and close actomyosin rings around Xenopus oocyte wounds. *J Cell Biol,* 154, 785-97.

Mandato, C. A. & Bement, W. M. 2003. Actomyosin transports microtubules and microtubules control actomyosin recruitment during Xenopus oocyte wound healing. *Curr Biol,* 13, 1096-105.

Matov, A., Applegate, K., Kumar, P., Thoma, C., Krek, W., Danuser, G. & Wittmann, T. 2010. Analysis of microtubule dynamic instability using a plus-end growth marker. *Nat Methods,* 7, 761-8.

Morris, R. L. & Hollenbeck, P. J. 1995. Axonal transport of mitochondria along microtubules and F-actin in living vertebrate neurons. *J Cell Biol,* 131, 1315-26.

Nangaku, M., Sato-Yoshitake, R., Okada, Y., Noda, Y., Takemura, R., Yamazaki, H. & Hirokawa, N. 1994. KIF1B, a novel microtubule plus end-directed monomeric motor protein for transport of mitochondria. *Cell,* 79, 1209-20.

Palazzo, A. F., Cook, T. A., Alberts, A. S. & Gundersen, G. G. 2001. mDia mediates Rho-regulated formation and orientation of stable microtubules. *Nat Cell Biol,* 3, 723-9.

Pathak, D., Sepp, K. J. & Hollenbeck, P. J. 2010. Evidence that myosin activity opposes microtubule-based axonal transport of mitochondria. *J Neurosci,* 30, 8984-92.

Pollard, T. D. & Cooper, J. A. 2009. Actin, a central player in cell shape and movement. *Science,* 326, 1208-12.

Portran, D., Schaedel, L., Xu, Z., Thery, M. & Nachury, M. V. 2017. Tubulin acetylation protects long-lived microtubules against mechanical ageing. *Nat Cell Biol,* 19, 391-398.

Reed, N. A., Cai, D., Blasius, T. L., Jih, G. T., Meyhofer, E., Gaertig, J. & Verhey, K. J. 2006. Microtubule acetylation promotes kinesin-1 binding and transport. *Curr Biol,* 16, 2166-72.

Rodriguez, O. C., Schaefer, A. W., Mandato, C. A., Forscher, P., Bement, W. M. & Waterman-Storer, C. M. 2003. Conserved microtubule-actin interactions in cell movement and morphogenesis. *Nat Cell Biol,* 5, 599-609.

Rotty, J. D., Wu, C. & Bear, J. E. 2013. New insights into the regulation and cellular functions of the ARP2/3 complex. *Nat Rev Mol Cell Biol,* 14, 7-12.

Rotty, J. D., Wu, C., Haynes, E. M., Suarez, C., Winkelman, J. D., Johnson, H. E., Haugh, J. M., Kovar, D. R. & Bear, J. E. 2015. Profilin-1 serves as a gatekeeper for actin assembly by Arp2/3-dependent and -independent pathways. *Dev Cell,* 32, 54-67.

Schuler, M. H., Lewandowska, A., Caprio, G. D., Skillern, W., Upadhyayula, S., Kirchhausen, T., Shaw, J. M. & Cunniff, B. 2017. Miro1-mediated mitochondrial positioning shapes intracellular energy gradients required for cell migration. *Mol Biol Cell,* 28, 2159-2169.

Sheng, Z. H. & Cai, Q. 2012. Mitochondrial transport in neurons: impact on synaptic homeostasis and neurodegeneration. *Nat Rev Neurosci,* 13, 77-93.

Shyu, Y. J., Liu, H., Deng, X. & Hu, C. D. 2006. Identification of new fluorescent protein fragments for bimolecular fluorescence complementation analysis under physiological conditions. *Biotechniques,* 40, 61-6.

Song, Y. & Brady, S. T. 2015. Post-translational modifications of tubulin: pathways to functional diversity of microtubules. *Trends Cell Biol,* 25, 125-36.

Song, Y., Kirkpatrick, L. L., Schilling, A. B., Helseth, D. L., Chabot, N., Keillor, J. W., Johnson, G. V. & Brady, S. T. 2013. Transglutaminase and polyamination of tubulin: posttranslational modification for stabilizing axonal microtubules. *Neuron,* 78, 109-23.

Suraneni, P., Rubinstein, B., Unruh, J. R., Durnin, M., Hanein, D. & Li, R. 2012. The Arp2/3 complex is required for lamellipodia extension and directional fibroblast cell migration. *J Cell Biol,* 197, 239-51.

Uruno, T., Liu, J., Zhang, P., Fan, Y., Egile, C., Li, R., Mueller, S. C. & Zhan, X. 2001. Activation of Arp2/3 complex-mediated actin polymerization by cortactin. *Nat Cell Biol,* 3, 259-66.

Wang, C., Du, W., Su, Q. P., Zhu, M., Feng, P., Li, Y., Zhou, Y., Mi, N., Zhu, Y., Jiang, D., Zhang, S., Zhang, Z., Sun, Y. & Yu, L. 2015. Dynamic tubulation of mitochondria drives mitochondrial network formation. *Cell Res,* 25, 1108-20.

Waterman-Storer, C. M., Worthylake, R. A., Liu, B. P., Burridge, K. & Salmon, E. D. 1999. Microtubule growth activates Rac1 to promote lamellipodial protrusion in fibroblasts. *Nat Cell Biol,* 1, 45-50.

Weaver, A. M., Karginov, A. V., Kinley, A. W., Weed, S. A., Li, Y., Parsons, J. T. & Cooper, J. A. 2001. Cortactin promotes and stabilizes Arp2/3-induced actin filament network formation. *Curr Biol,* 11, 370-4.

Wittmann, T., Bokoch, G. M. & Waterman-Storer, C. M. 2003. Regulation of leading edge microtubule and actin dynamics downstream of Rac1. *J Cell Biol,* 161, 845-51.

Wittmann, T. & Waterman-Storer, C. M. 2001. Cell motility: can Rho GTPases and microtubules point the way? *J Cell Sci,* 114, 3795-803.

Wu, C., Asokan, S. B., Berginski, M. E., Haynes, E. M., Sharpless, N. E., Griffith, J. D., Gomez, S. M. & Bear, J. E. 2012. Arp2/3 is critical for lamellipodia and response to extracellular matrix cues but is dispensable for chemotaxis. *Cell,* 148, 973-87.

Xu, Z., Schaedel, L., Portran, D., Aguilar, A., Gaillard, J., Marinkovich, M. P., Thery, M. & Nachury, M. V. 2017. Microtubules acquire resistance from mechanical breakage through intralumenal acetylation. *Science,* 356, 328-332.

Zhang, X., Yuan, Z., Zhang, Y., Yong, S., Salas-Burgos, A., Koomen, J., Olashaw, N., Parsons, J. T., Yang, X. J., Dent, S. R., Yao, T. P., Lane, W. S. & Seto, E. 2007. HDAC6 modulates cell motility by altering the acetylation level of cortactin. *Mol Cell,* 27, 197-213.

Zhang, Z., Nishimura, Y. & Kanchanawong, P. 2017. Extracting microtubule networks from superresolution single-molecule localization microscopy data. *Mol Biol Cell,* 28, 333-345.
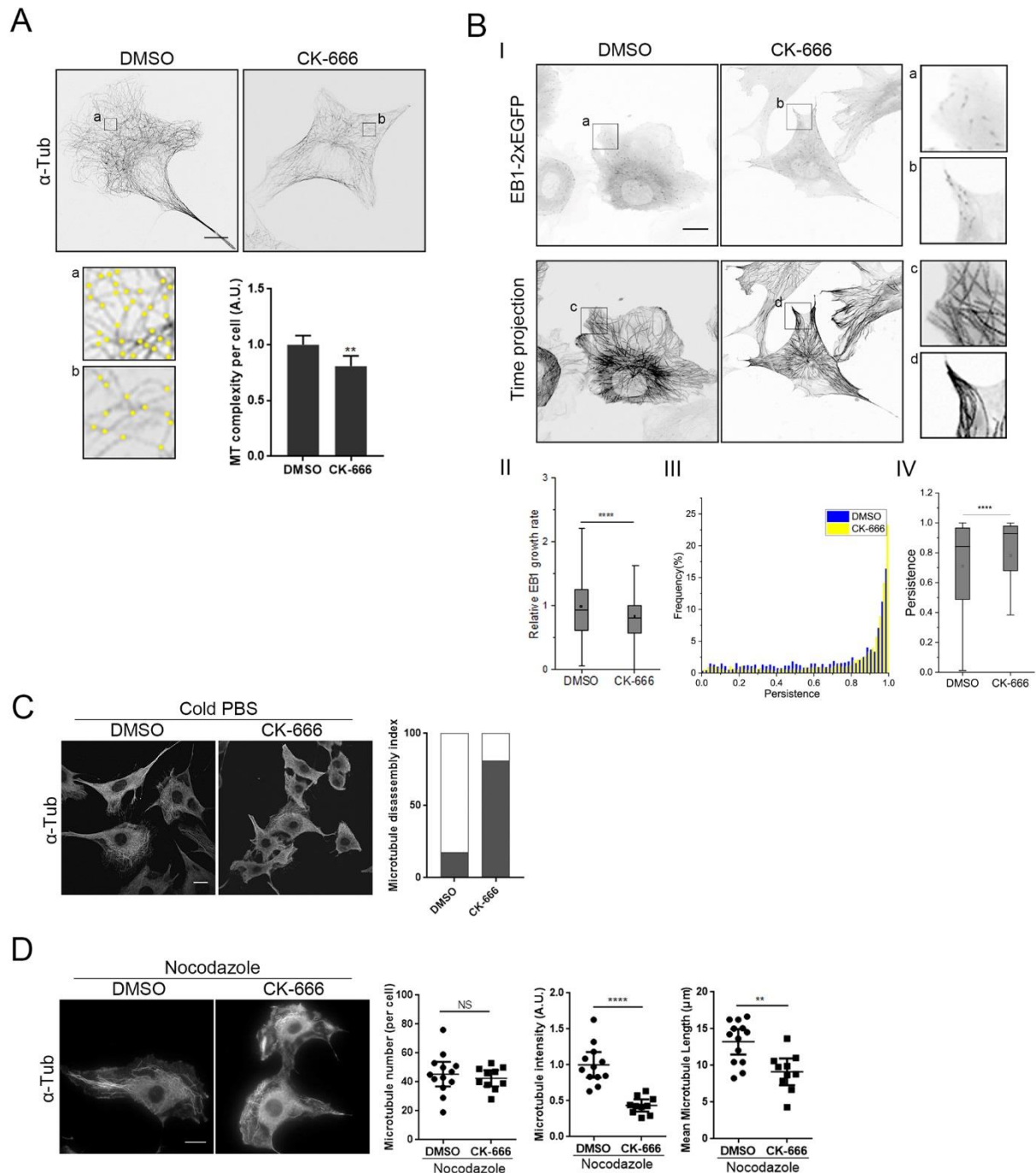
Figures

Figure 1. Disruption of the branched actin affects microtubule complexity, dynamics and stability.

(A) Representative immunofluorescent images of α-tubulin in mouse embryonic fibroblasts (MEFs) under DMSO or 100 µM CK-666 treatment for 6 h. Cells were fixed with -20 ℃ pre-chilled methanol. Images were captured using an LSM 880 Airyscan with Axio Observer Z1 (Objective: Plan-Apo 63/1.4). Microtubule joints were illustrated as the yellow dots in the zoomed boxes (labelled as a and b) showed the illustration of microtubule

joint. The mean joint numbers under DMSO and CK-666 are about 223 and 180 per 100 μm^2. Numbers of microtubule joints per cells were quantified and plotted as microtubule complexity (mean ± 95% CI). N_{DMSO} =34, N_{CK-666} =30, **, P=0.002, by Student's t test. Scale bar: 5 μm.

(B) I: Upper pannel: representative images of MEFs expressing EB1 fused with 2×EGFP (EB1-2xEGFP) under DMSO or 100 μM CK-666 for 6 h. Bottom panel: the time projection of movies related to the upper panel. The enlarged boxes showed the detail structure. II: box plots showing the relative speed of EB1, as tracked and analyzed with plusTipTracker software. III & IV: The frequency distribution and box plot of cell edge EB1 persistence was plotted. For box plots, 25th percentile (bottom boundary), median (middle line), and 75th percentile (top boundary) were indicated. 5 cells (each distribution comprises n > 3000 measurements) were analyzed under each condition by non-parameter test (see methods). EB1 dots were tracked and persistence was calculated as the ratio of L/S (L: the distance from start to end; S: the sum of accumulated distance). Scale bar: 20 μm.

(C) Representative immunofluorescent staining of α-tubulin under DMSO or 100 μM CK-666 for 6 h and followed by 4 ℃cold PBS for 20 min. N_{DMSO} = 161, N_{CK-666}=155. The percentage of microtubule disassembled cells was plotted. Scale bar: 20 μm.

(D) Representative immunofluorescent staining of α-tubulin of MEFs under DMSO or 100 μM CK-666 treatment for 6 h, followed by 8 μM nocodazole treatment for 5 min. Integrated microtubule fluorescent density, microtubule numbers and mean microtubule length were quantified by image J and plotted as mean ± 95% CI. N_{DMSO} =13, N_{CK-666} =10. ****, P<0.0001, by Student's t test. Scale bar: 20 μm.
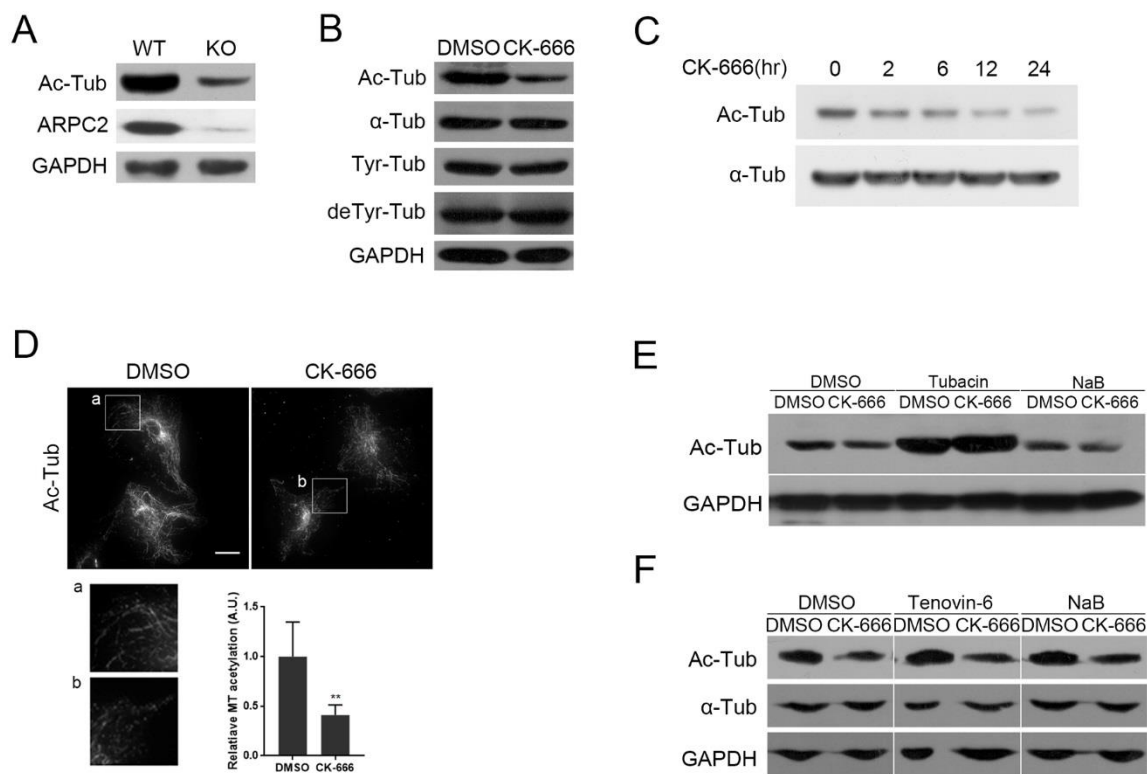
Figure 2. Perturbation of the Arp2/3-branched actin affects microtubule acetylation level through HDAC6.

(A) Western blot showing acetylated tubulin level in wild-type (WT) and ARPC2 knockout (ARPC2 KO) MEFs. Ac-Tub: acetylated-α-tubulin. GAPDH used as a loading control.

(B) Western blot showing acetylated tubulin, tyrosinated tubulin and detyrosinated tubulin levels in MEFs treated with DMSO or 100 μM CK-666 treatment for 6 h. Tyr-Tub: Tyrosinated-α-tubulin, deTyr-Tub: non-tyrosinated-α-tubulin. GAPDH used as a loading control.

(C) Western blot showing acetylated tubulin level with 100 μM CK-666 treatment at different time points. α-tubulin used as loading control.

(D) Representative immunofluorescence images stained with acetylated-α-tubulin in MEFs treated with DMSO or CK-666 for 6 h. Integrated pixel density per cell was quantified and plotted as mean ± 95% CI (N_{DMSO}=18, N_{CK-666}=13). ∗∗, P=0.006, by Student's t test. Scale bar: 20 μm.

(E) Western blot showing the acetylated tubulin level in MEFs under indicated treatments for 6 h. CK-666: 100 μM, Tubacin: 10 μM, NaB: 5 mM. GAPDH used as a loading control.

(F) Western blot showing acetylated tubulin level in MEFs under indicated treatments for 6 h. Tenovin-6: 20 μM, NaB: 5 mM. GAPDH used as a loading control.
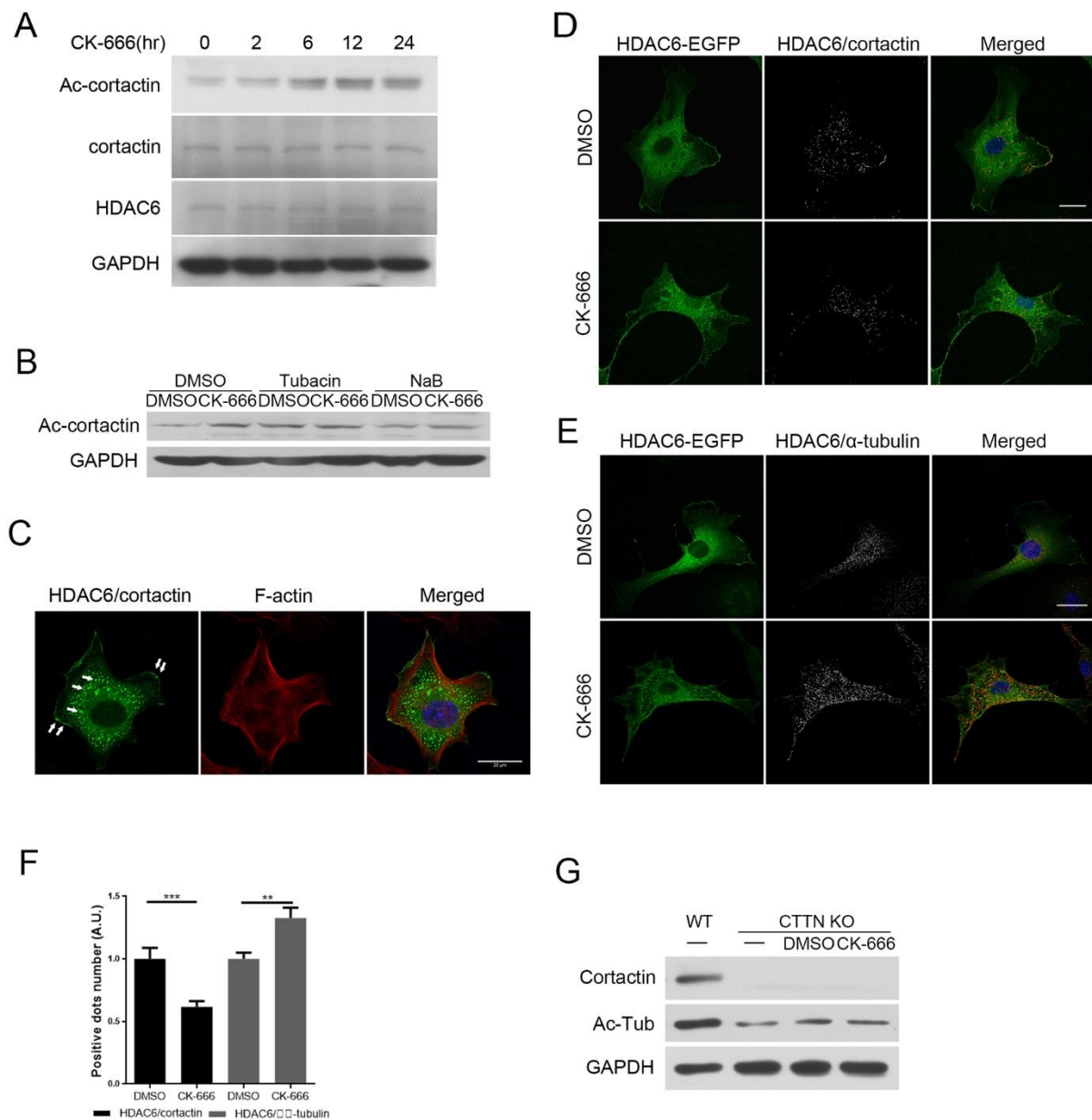
Figure 3. HDAC6 balances cortactin and tubulin acetylation levels to orchestrate branched actin and microtubule cytoskeletons.

(A) Western blot showing the acetylated cortactin, total cortactin and HDAC6 levels in MEFs under 100 μM CK-666 treatment at different time points. GAPDH used as a loading control.

(B) Western blot showing the acetylated cortactin level in MEFs under indicated treatments for 6 h. CK-666: 100 μM, Tubacin: 10 μM, NaB: 5 mM. GAPDH used as a loading control.

(C) Representative image of HDAC6-cortactin BiFC assay. HDAC6-VN173 and cortactin-VC155 were co-transfected into MEFs. Scale bar: 20 μm.

(D) Representative images of the proximity ligation assay (in situ PLA) between HDAC6-EGFP and cortactin. Scale bar: 20 μm.

(E) Representative images of the proximity ligation assay (in situ PLA) between HDAC6-EGFP and α-tubulin. Scale bar: 20 µm.

(F) Positive dots per cell in D and E were quantified and plotted as mean ± SEM. D: N_{DMSO}=20, N_{CK-666}=22, ***, p=0.0003 by Student's *t* test and E: N_{DMSO}=22, N_{CK-666}=17, **, p=0.004 by Student's *t* test.

(G) Western blot showing acetylated α-tubulin level in wild type (WT) and cortactin knockout (CTTN KO) MEFs under DMSO or 100 µM CK-666 treatment for 6 h. GAPDH used as a loading control.
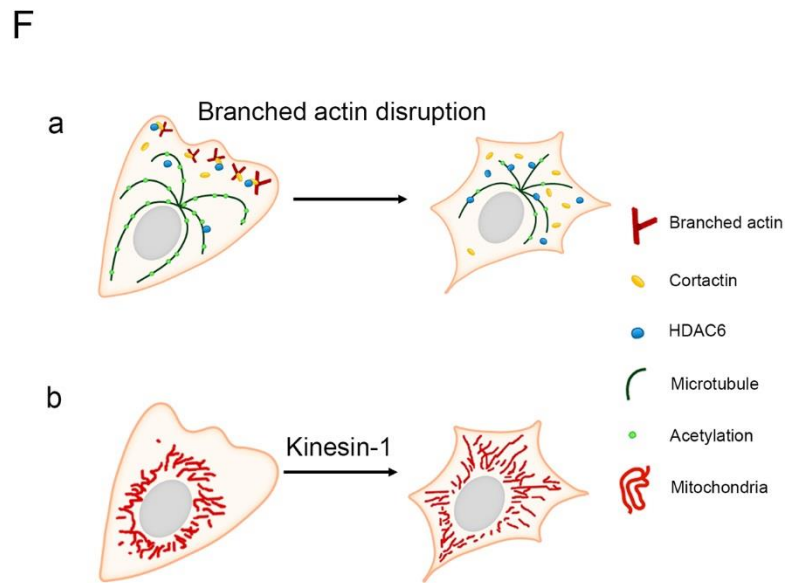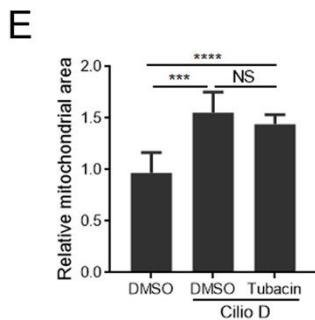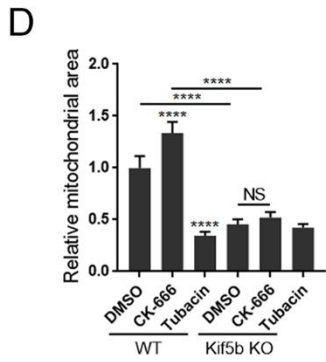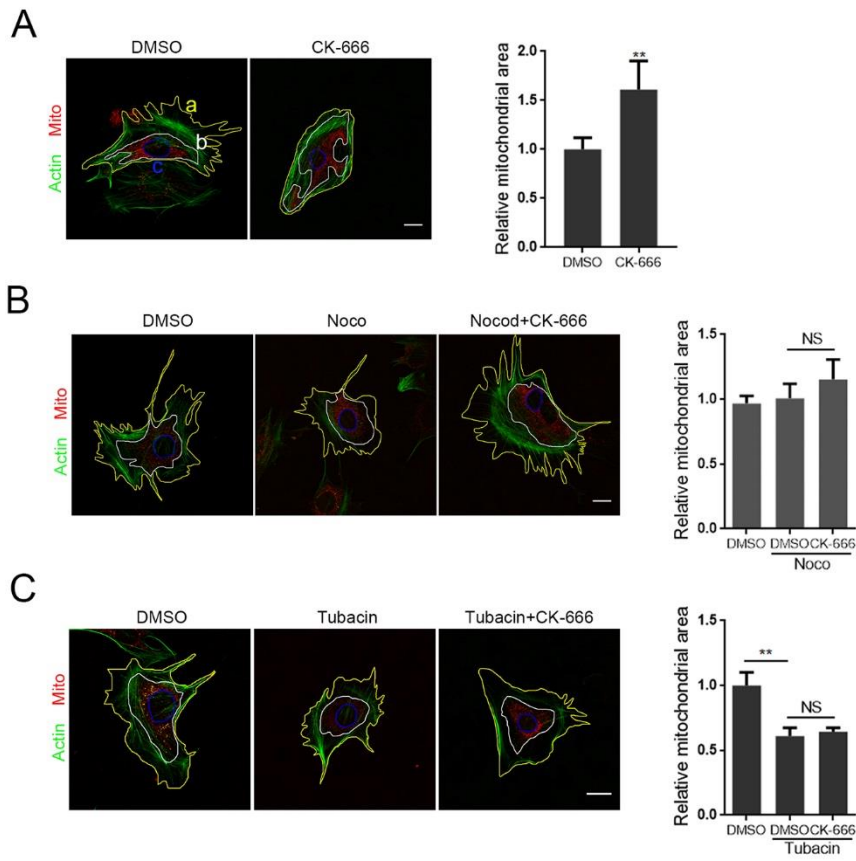
Figure 4. Arp2/3-branched actin regulates mitochondria disruption through changes in microtubule acetylation level.

(A) Representative immunofluorescence images stained with mitotracker and phalloidin in MEFs treated with DMSO or 100 µM CK-666 for 6 h. Yellow outline indicates cell boundary (a); white outline indicates the boundary of mitochondrial network (b) and blue outline indicates the nuclear boundary (c). Mitochondrial percentage equals the mitochondiral area subtracted the nuclear area then divided by the total cytoplasmic area. Mitochondria percentage=area of (b-c)/ area of a. Mitochondrial area was quantified and plotted as mean ± 95% CI. ∗∗, p=0.0017 by Student's t test, $N_{control}$ =7, N_{CK-666}=10. Scale bar: 20 µm.

(B) Representative immunofluorescence images stained with mitotracker and phalloidin in MEFs treated with 33 µM nocodazole for 3 h, followed by 100 µM CK-666 treatment for 6 h. Mitochondrial area was quantified and plotted as mean ±95% CI. NS, p=0.4826 by Student's t test, , $N_{control}$ =6, $N_{Nocodazole}$ =7, $N_{Nocodazole+CK-666}$=5. Scale bar: 20 µm.

(C) Representative immunofluorescence images stained with mitotracker and phalloidin in MEFs treated with 10 µM Tubacin or 10 µM Tubacin combined with 100 µM CK-666 for 6 h. Mitochondrial percentage per cell was quantified and plotted as mean ± 95% CI. ∗∗, p=0.0081, NS, p=0.6968 by Student's t test, $N_{control}$=6, $N_{Tubacin}$=6, $N_{Tubacin+CK-666}$ =4. Scale bar: 20 µm.

(D) Histogram showed mitochondrial area of WT and Kif5b knockout RPE cells treated with DMSO, 100 µM CK-666 for 4 h or 10 µM Tubacin for 6 h. Mitochondrial area per cell was quantified and plotted as mean ±95% CI. ∗∗∗∗, p<0.0001 by Student's t test, RPE WT cells: N_{DMSO}=25, N_{CK-666}=26, $N_{Tubacin}$=21. RPE Kif5b KO cells: N_{DMSO}=15, N_{CK-666}=23, $N_{Tubacin}$=30.

(E) Histogram showed mitochondrial area of MEF cells under DMSO, 10 µM Tubacin for 6h or 50 µM Ciliobrevins D treatment for 1.5 h. The relative mitochondiral area per cell was quantified and plotted as mean ± SEM. p=0.0001 by Student's t test, N_{DMSO} =11, $N_{Cilio\ D}$=19, $N_{Cilio\ D+Tubacin}$=21.

(F) Schematic model showing the effects of Arp2/3-branched actin perturbation on tubulin acetylation level and mitochondria distribution. (a)Arp2/3-branched actin maintains cortactin localization at the cell leading edge and facilitates cortactin-HDAC6 interaction. Upon branched actin disruption, cortactin dissociates from the cell periphary and translocates to the cytoplasm. Meanwhile, cortactin-HDAC6 interaction decreases while tubulin-HDAC6 affinity increases. (b)Arp2/3-branched actin confines mitochondria distribution by maintaining the microtubule acetylation level. When the Arp2/3 complex is perturbed, mitochondria meshwork expands, probably due to imbalanced trafficking of kinesin and dynein motors.
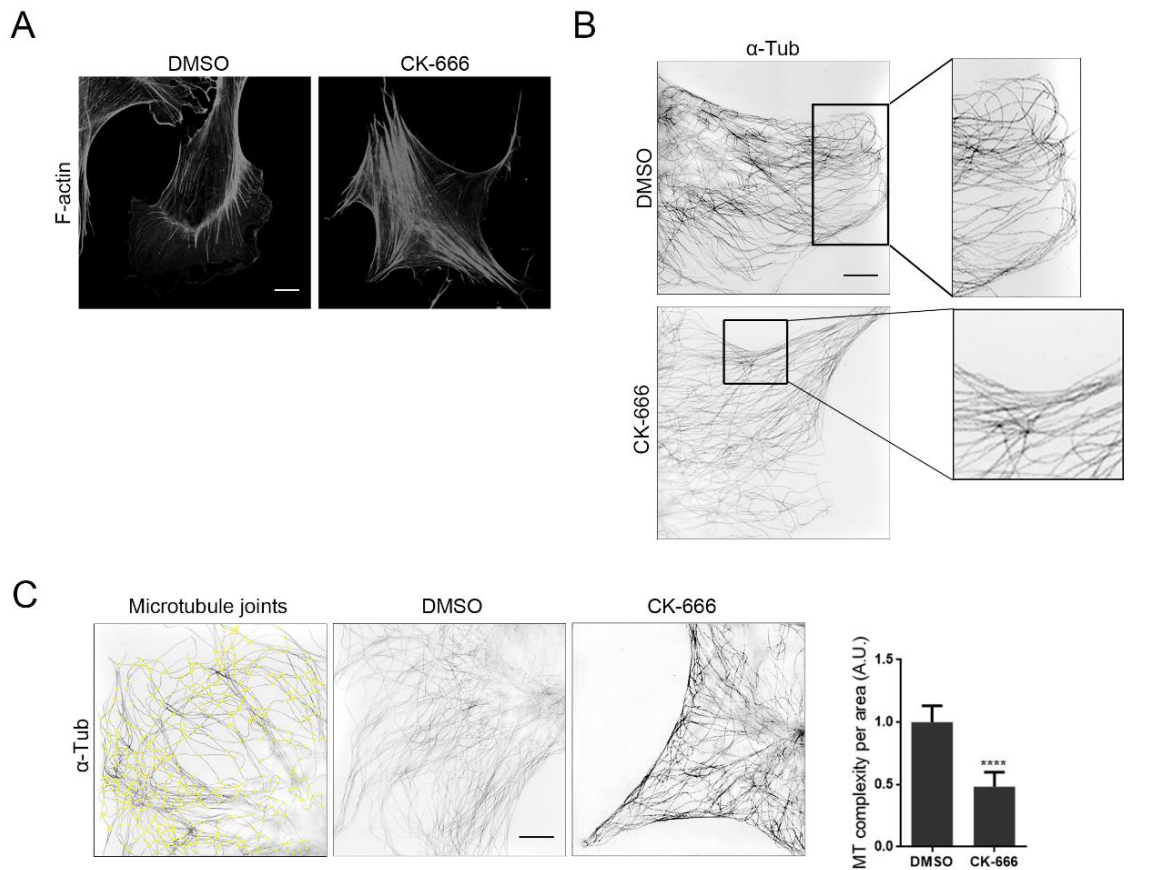
Figure S1. The architecture of actin and microtubule network.

(A) Representative flurocent images of F-actin in MEFs under DMSO, 100 μM CK-666 treatment for 6 h. Scale bar: 20 μm.

(B) Representative immunoflurocent images of α-tubulin in MEFs under DMSO, 100 μM CK-666 treatment for 6 h, captured by Structured Illumination Microscopy (SIM). The enlarged boxes showed microtubule network at the cell leading edge. Scale bar: 5 μm.

(C) The illustration of microtubule joints and representative immunoflurocent images of α-tubulin in MEFs under DMSO, 100 μM CK-666 treatment for 6 h. Images were captured by SIM. Scale bar: 20 μm. Five views were analyzed under each condition. Numbers of filament interconnections per area were quantified and plotted as microtubule complexity (mean ± 95%CI). ∗∗∗∗, P<0.0001, by Student's *t* test. Scale bar: 5 μm.
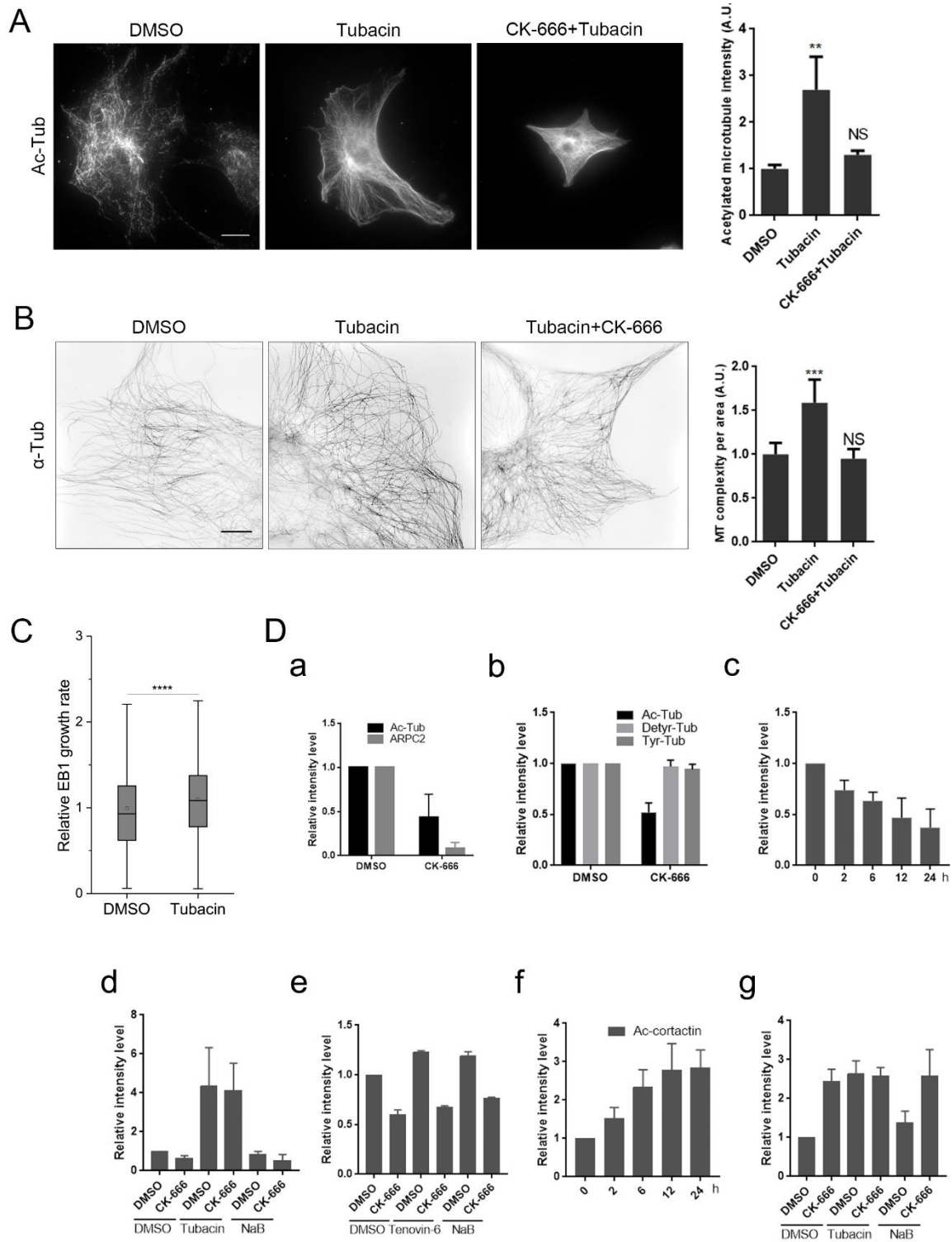
Figure S2. The dynamic and organization of microtubule response to altered microtubule acetylation.

(A) Representative immunoflurocent images of acetylated α-tubulin in MEFs under DMSO, 100 μM CK-666, or 10 μM Tubacin treatment for 6 h. Acetylated microtubule intensity was quantified and plotted (mean ± SEM).

N_{DMSO}=13, $N_{Tubacin}$=5, $N_{Tubacin+CK-666}$=5. Scale bar: 20 μm.

(B) Representative images of microtubule captured by SIM under DMSO, 10 μM Tubacin or 100 μM CK-666 plus 10 μM Tubacin treatment for 6 h. Five cells were analyzed under each condition. Numbers of filament interconnections per area were quantified and plotted as microtubule complexity (mean ± 95% CI). ∗∗∗, P=0.0002, by Student's *t* test. Scale bar: 5 μm.

(C) Microtubule dynamic under DMSO and 10 μM Tubacin treatment for 6 h. Box plots showing the relative speed of EB1, as tracked and analyzed with plusTipTracker software. 25th percentile (bottom boundary), median (middle line), and 75th percentile (top boundary) were indicated. 5 cells were analyzed under each condition by non-parameter test.

(D) The quantification of western blotting related to Figure 2 and Figure 3. Histograms a to e related to the Figures 2A, 2B, 2C 2E and 2F. Histogram f and g related to the Figure 3A and 3B. The intensity of bands was quantified by using Image J (Image J ⟶ Analyze⟶Gels). For each histogram, three independent assays and measurements were done.
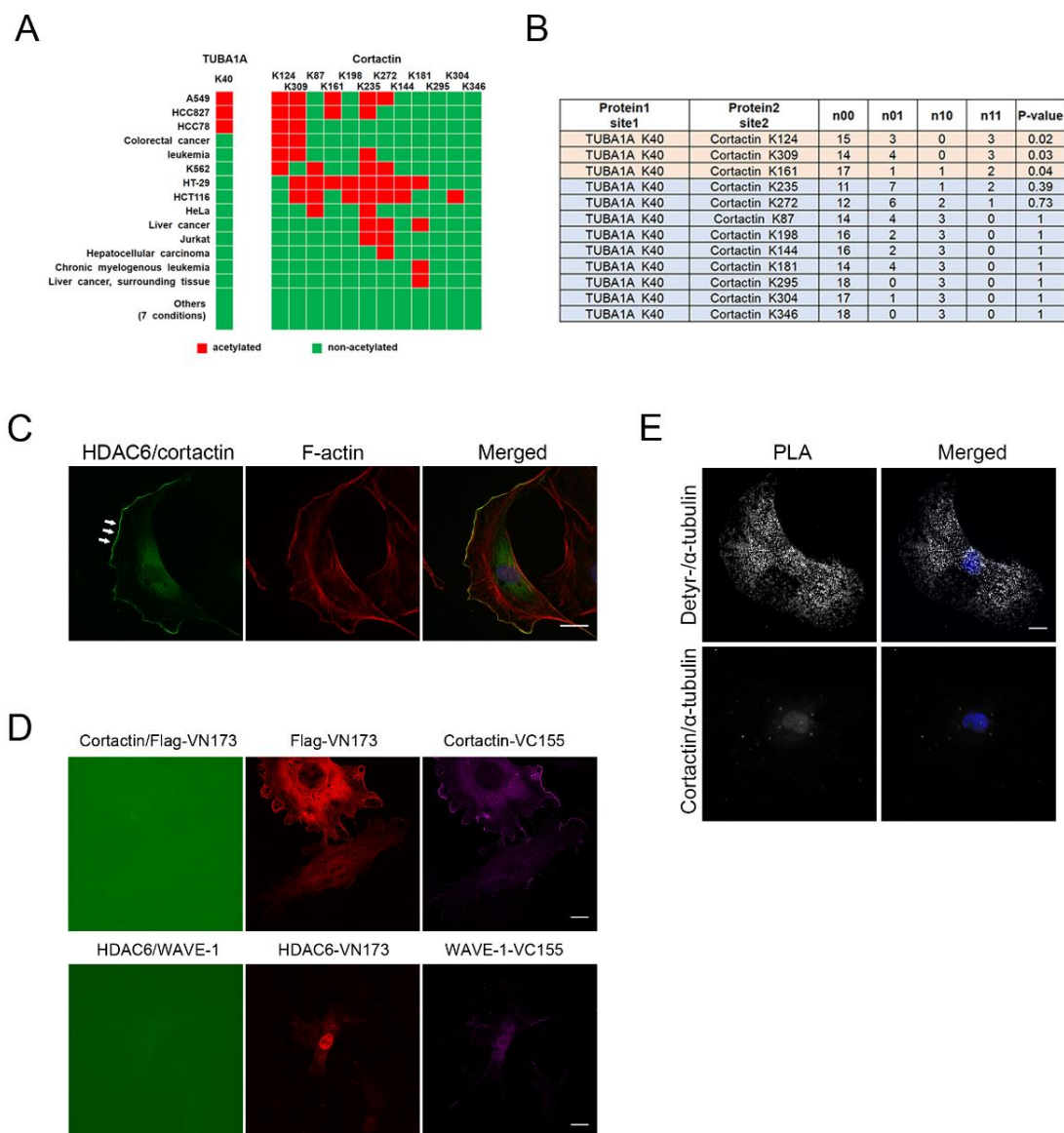
B

Protein1 site1	Protein2 site2	n00	n01	n10	n11	P-value
TUBA1A K40	Cortactin K124	15	3	0	3	0.02
TUBA1A K40	Cortactin K309	14	4	0	3	0.03
TUBA1A K40	Cortactin K161	17	1	1	2	0.04
TUBA1A K40	Cortactin K235	11	7	1	2	0.39
TUBA1A K40	Cortactin K272	12	6	2	1	0.73
TUBA1A K40	Cortactin K87	14	4	3	0	1
TUBA1A K40	Cortactin K198	16	2	3	0	1
TUBA1A K40	Cortactin K144	16	2	3	0	1
TUBA1A K40	Cortactin K181	14	4	3	0	1
TUBA1A K40	Cortactin K295	18	0	3	0	1
TUBA1A K40	Cortactin K304	17	1	3	0	1
TUBA1A K40	Cortactin K346	18	0	3	0	1

Figure S3. Co-occurrence analysis and Cortactin-HDAC6 interation.

 (A) and (B) Co-occurrence analysis of the acetylation site on TUBA1A (K40) and acetylation sites on cortactin (K124, K309, K87 et al.). The acetylation status (red: on, green: off) across 21 conditions were shown. For each pairwise combination of acetylation site, their joint acetylation status was summarized into a contingency table with four entries nij (i, j ∈ $\{0,1\}$), where nij denotes the number of times the site 1 is in state i site 2 is in state j. One-sided FET was used to test if two sites were acetylated together more frequntly than expected. The pairs with FET p-value < 0.05 were highlighted.

(C) Representative BiFC imaes of HDAC/cortactin, HDAC6/WAVE1 and Cortactin/VN-173 sgnals. Scale bar: 20μm.

(D) The representative images of positive and negative control in PLA assay. Detyr-Tub and α-tubulin were used as positive control. Cortactin and α-tubulin were used as negative control. Scale bar: 20μm.
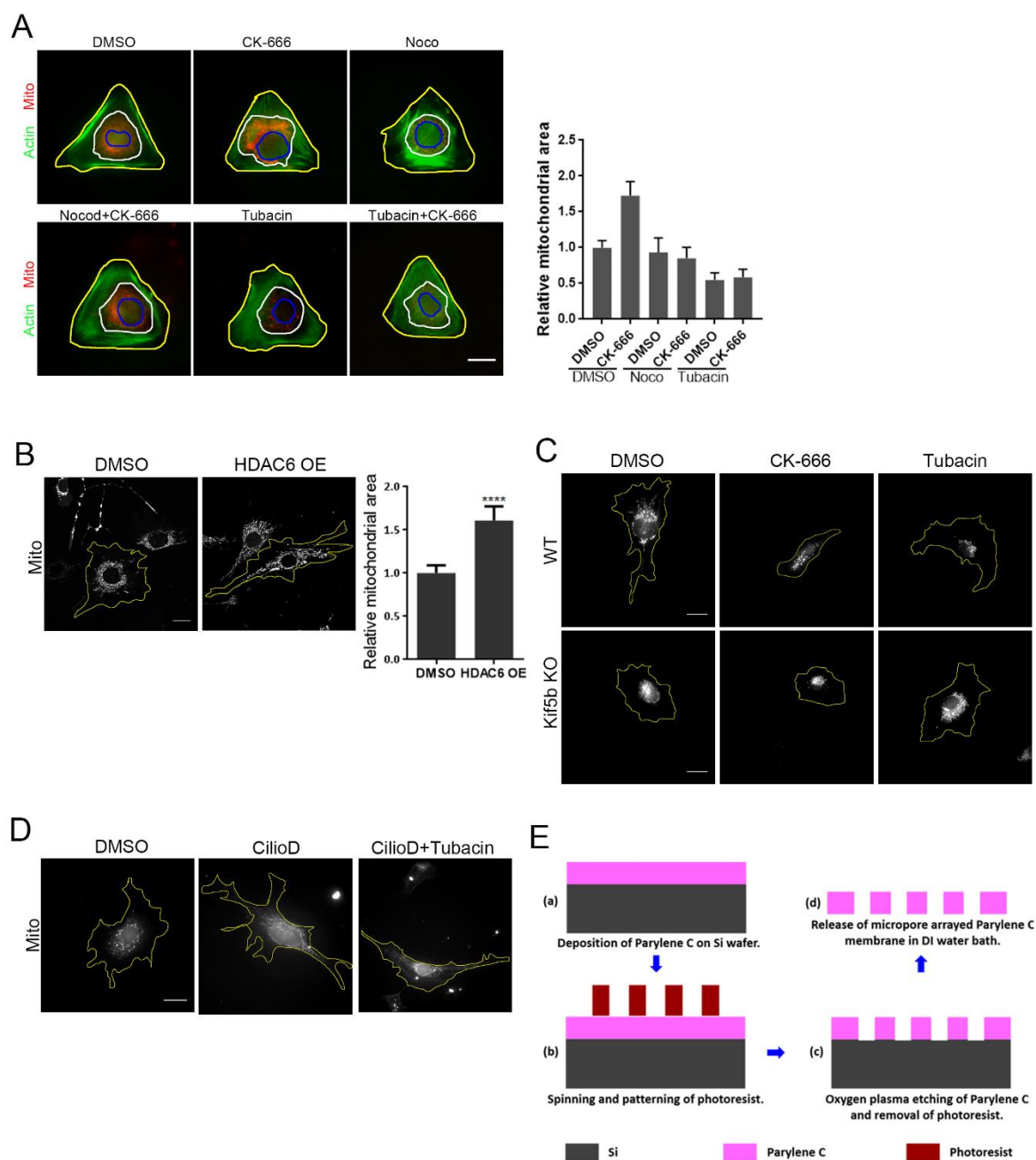
**Figure S4. Mitochondrial distribution alteration response to microtubule acetylation.**

(A) Representative images of cells stained for F-actin and mitochondria under the spreading into equilateral triangular shape of 2000 μm^2. Mitochondrial area was quantified and plotted as mean ± 95% CI. P<0.0001 by Student's *t* test, N_{DMSO} =20, N_{CK-666}=8, $N_{DMSO+Noco}$ =12, $N_{Noco+CK}$-666 =14, $N_{DMSO+Tubacin}$ =10, $N_{Tubacin+CK-666}$ =20. Scale bar: 20 μm.

(B) Representative images of WT and HDAC6 overexpresing MEFs stained for mitochondria. Mitochondrial area per cell was quantified and plotted as mean ± 95%CI. ****, p<0.0001, by Student's t test, $N_{Control}$=12, $N_{HDAC6\ OE}$=16. Scale bar: 20 μm.

(C) Representative immunofluorescence images stained for F-actin and mitochondria in RPE WT or Kif5b KO RPE cells treated with DMSO or 100 µM CK-666 treatment for 6h, or 10 µM Tubacin for 6 h. Scale bar: 20 µm.

(D) Representative images of cells stained forF-actin and mitochondria under DMSO, 10 µM Tubacin treatment for 6 h or 50 µM Cilio D treatment for 1.5 h. Scale bar: 20 µm.

(E) The schematic of fabrication process for the micropore-arrayed Parylene C membrane.
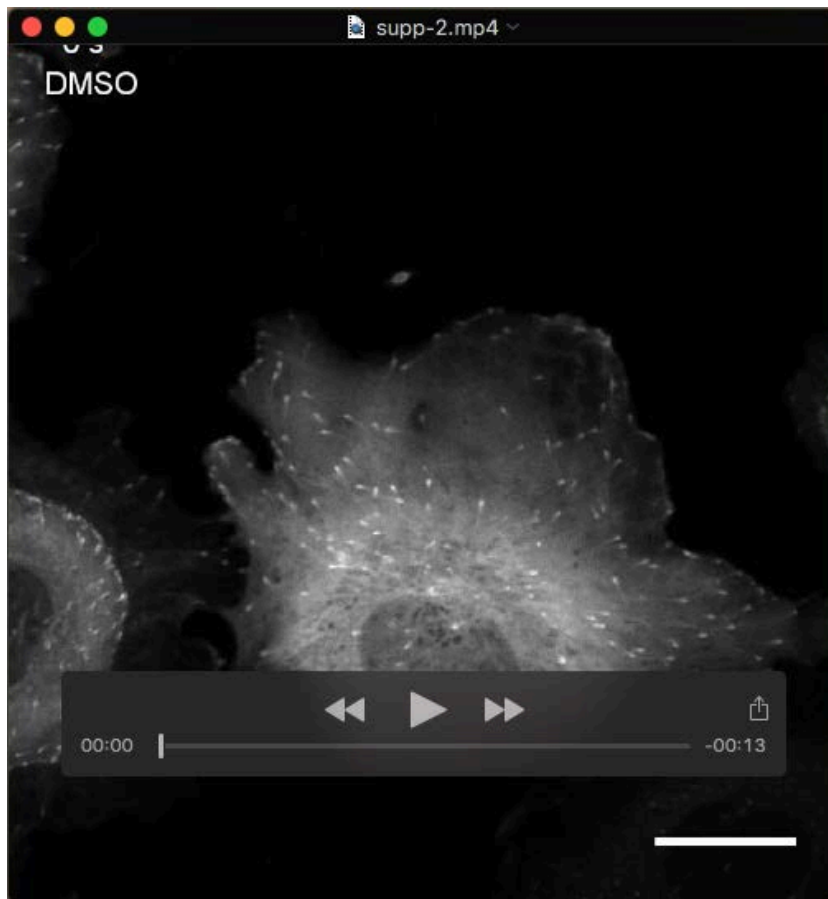
Movie 1. Microtubule dynamics under DMSO treatment. Time-lapse movies of MEFs stably expressing EB1-2×EGFP under DMSO treatment for 6 h. Time interval: 2 s, total time: 3 min, scale bar: 20 µm.
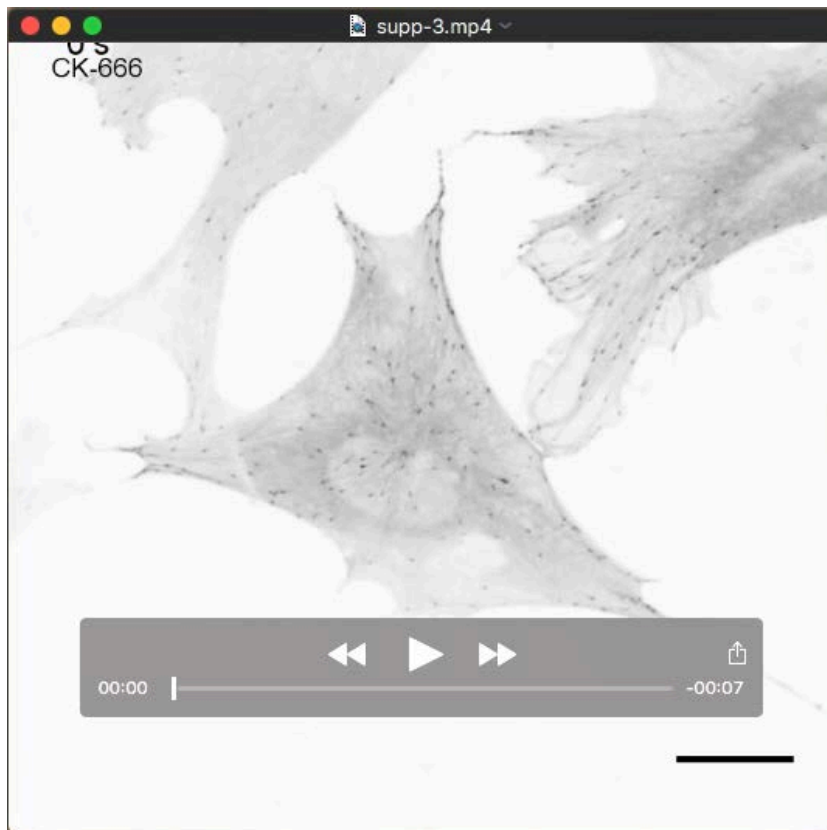
Movie 2. Microtubule dynamics CK-666 treatment. Time-lapse movies of MEFs stably expressing EB1-2×EGFP under 100 µM CK-666 Tubacin treatment for 6 h. Time interval: 2 s, total time: 3 min, scale bar: 20 µm.
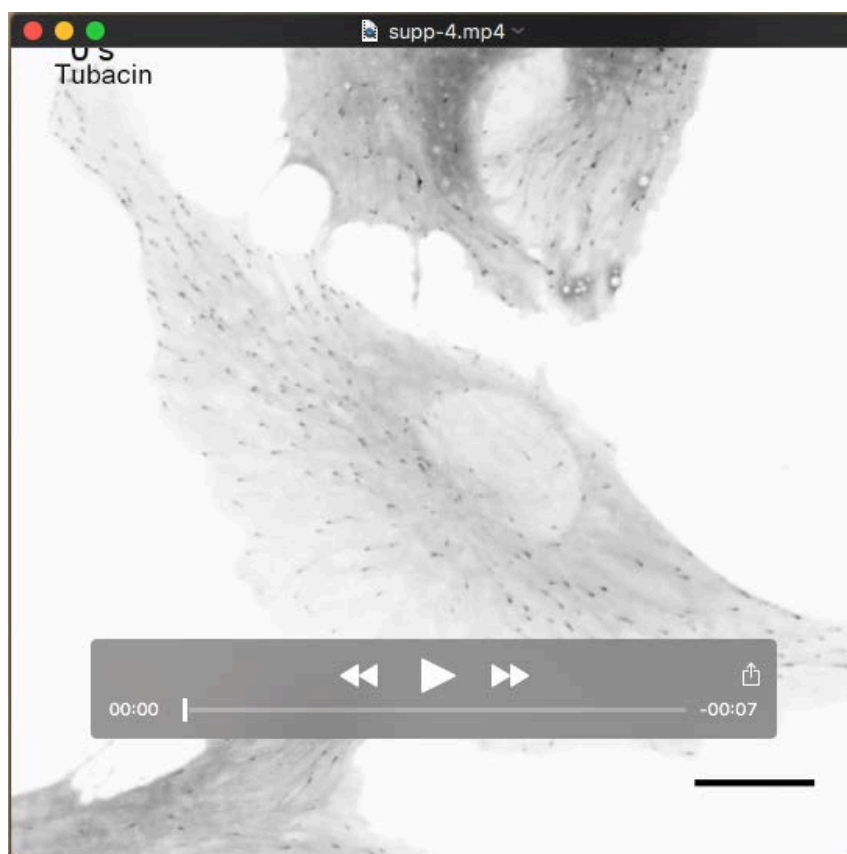
Movie 3. Microtubule dynamics under Tubacin treatment. Time-lapse movies of MEFs stably expressing EB1-2×EGFP under 10 µM Tubacin treatment for 6 h. Time interval: 2 s, total time: 3 min, scale bar: 20 µm.
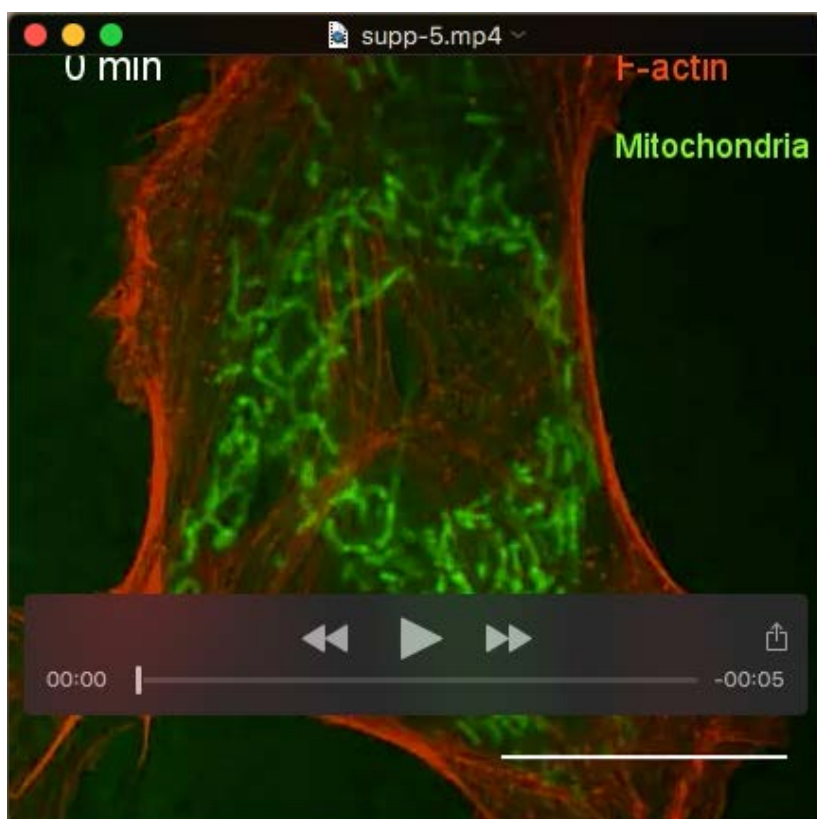
Movie 4. Mitochondrial distribution under DMSO treatment. Time-lapse movies of MEFs stained for F-actin and mitochondria under DMSO treatment. Time interval: 4 min, total time: 2 h. Scale bar: 20 μm.
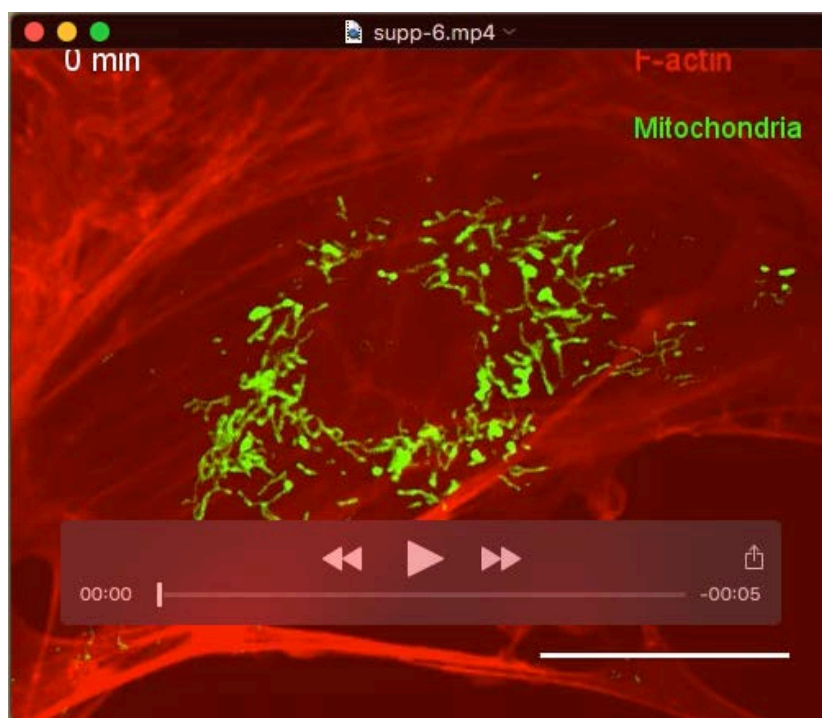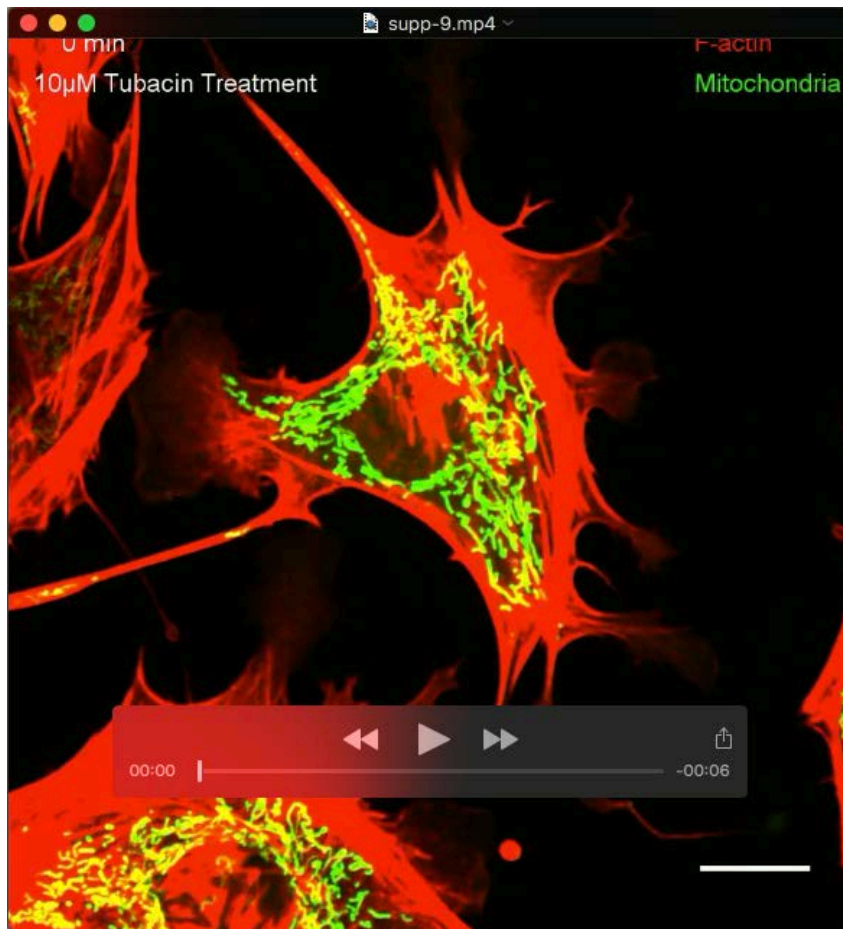
Movie 5. Mitochondrial distribution under CK-666 treatment. Time-lapse movies of MEFs stained for F-actin and mitochondria under 100 µM CK-666 treatment. Time interval: 6 min, total time: 2.5 h. Scale bar: 20 µm.
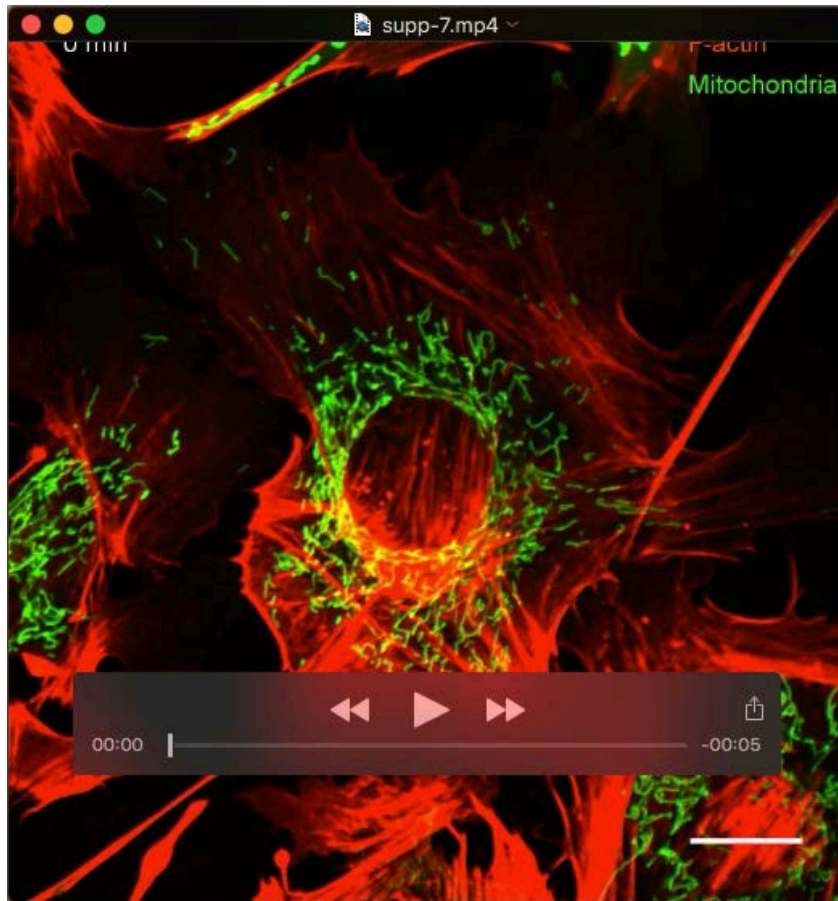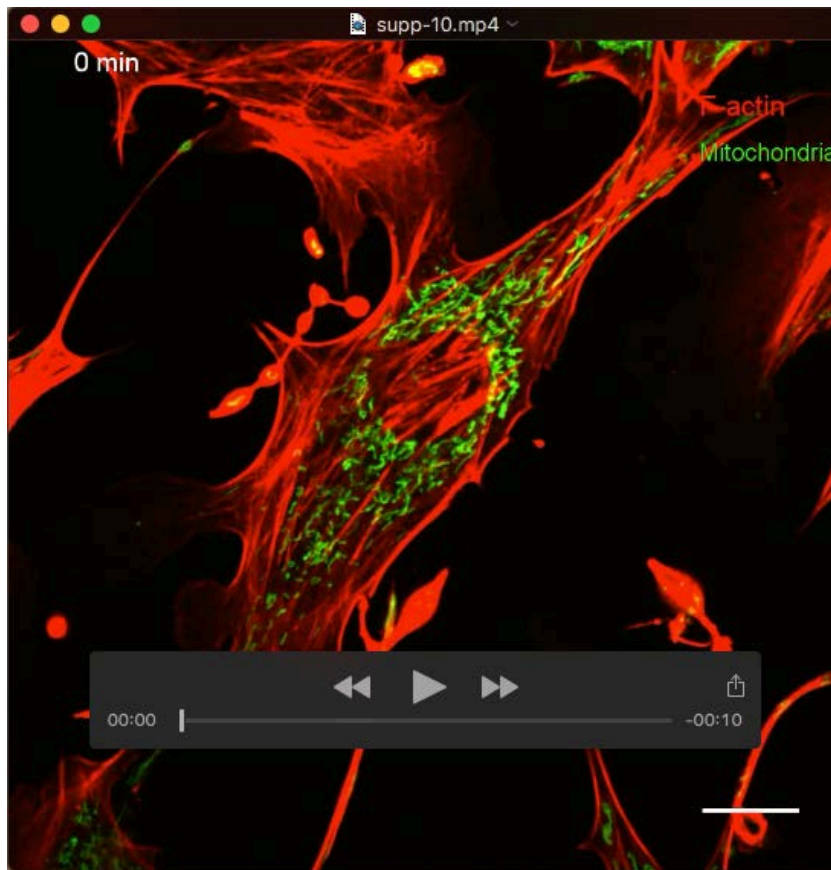
Movie 6. Mitochondrial distribution under Nocodazole treatment. Time-lapse movies of MEFs stably expressing mito-YFP and Lifeact-RFP under 33 µM nocodazole. Time interval: 5 min, total time: 2.5 h. Scale bar: 20 µm.

Movie 7. Mitochondrial distribution under Nocodazole and CK-666 treatment. Time-lapse movies of MEFs stably expressing mito-YFP and Lifeact-RFP under 33 µM nocodazole and 100 µM CK-666. Time interval: 5 min, total time: 3 h. Scale bar: 20 µm.

Movie 8. Mitochondrial distribution under Tubacin treatment. Time-lapse movies of MEFs stably expressing mito-YFP and Lifeact-RFP under 10 µM treatment. Time interval: 4 min, total time: 3.5 h. Scale bar: 20 µm.

Movie 9. Mitochondrial distribution under Tubacin and CK-666 treatment. Time-lapse movies of MEFs stably expressing mito-YFP and Lifeact-RFP under 10 µM Tubacin and 100 µM CK-666 treatment. Time interval: 5 min, total time: 5 h. Scale bar: 20 µm.